nature materials

ARTICLES

https://doi.org/10.1038/s41563-019-0452-y

Programming shape using kirigami tessellations

Gary P. T. Choi[1], Levi H. Dudte[1] and L. Mahadevan[1,2,3]*

Kirigami tessellations, regular planar patterns formed by partially cutting flat, thin sheets, allow compact shapes to morph into open structures with rich geometries and unusual material properties. However, geometric and topological constraints make the design of such structures challenging. Here we pose and solve the inverse problem of determining the number, size and orientation of cuts that enables the deployment of a closed, compact regular kirigami tessellation to conform approximately to any prescribed target shape in two or three dimensions. We first identify the constraints on the lengths and angles of generalized kirigami tessellations that guarantee that their reconfigured face geometries can be contracted from a non-trivial deployed shape to a compact, non-overlapping planar cut pattern. We then encode these conditions into a flexible constrained optimization framework to obtain generalized kirigami patterns derived from various periodic tesselations of the plane that can be deployed into a wide variety of prescribed shapes. A simple mechanical analysis of the resulting structure allows us to determine and control the stability of the deployed state and control the deployment path. Finally, we fabricate physical models that deploy in two and three dimensions to validate this inverse design approach. Altogether, our approach, combining geometry, topology and optimization, highlights the potential for generalized kirigami tessellations as building blocks for shape-morphing mechanical metamaterials.

Kirigami, the creative art of paper cutting and folding, and the tessellations derived from it have recently emerged as prototypical routes towards a new class of mechanical metamaterials. Indeed, various studies have focused on quantifying the geometry and kinematics of deployment of a given kirigami pattern, and their potential as auxetic structures and shape-morphing sheets[1–18], the so-called forward problem. From a mathematical, physical and a technological perspective, perhaps an even more interesting question is the inverse problem: can one design the kirigami tessellations in a closed, compact subset of the plane, so that it can be deployed into a prescribed final shape in two or three dimensions? Here, we pose this puzzle as a constrained optimization problem and solve it in a range of situations.

The simplest planar deployable kirigami patterns are based on periodic tilings of the plane using triangles, squares and hexagons, although other complex tessellations inspired by art and architecture have been explored recently[4,19]. Here we focus on using the quadrilateral kirigami pattern for ease of exposition; however, our methods generalize to any periodic pattern (see Supplementary Information, Section 1). In Fig. 1a, we show the quad tessellation of the plane in its compact and deployed state, with the cuts along the edges of the quads designed to allow for rotational in-plane deployment about a set of hinges. This pattern constitutes a one-degree-of-freedom mechanism whose planar deployment yields a continuous family of self-similar shapes that terminates at self-intersecting configurations. The basic unit cell underlying this pattern is also shown in Fig. 1a in both its undeployed and deployed states and shows the mathematical constraints that define the system: pairs of deployed edges contract to the same edge in the undeployed state, and simultaneously sets of deployed angles contract to the same single vertex in the undeployed state. Given an initially periodic tiling of a patch of the plane with this unit cell, we can state our inverse design problem thus (as shown in Fig. 1b): how should the unit cell be modulated in space to approximate a given planar shape in its deployed state and still be able to tile a patch of the Euclidean plane compactly when undeployed?

To find a solution requires us to search for potentially admissible results in the deployed space. A first step in this process is to quantify the constraints that will allow the deployed initialization geometry to correspond to a valid kirigami pattern that can compactly close onto a Euclidean patch. The necessary and sufficient contractibility conditions imply that a valid deployed configuration must be able to contract (undeploy) the configuration into a generalized kirigami pattern that closes consistently along the cuts without any mismatch or overlap in lengths and angles. As illustrated in Fig. 1b, the contractibility constraints are: (1) every pair of edges with edge lengths a, b in the deployed space that correspond to the same cut must satisfy the condition

$$a^2 - b^2 = 0 \tag{1}$$

(2) Every set of four angles in the deployed space that correspond to an interior node must sum to 2π, so that

$$\theta_1 + \theta_2 + \theta_3 + \theta_4 = 2\pi \tag{2}$$

where θ_i are angles in the deployed space as illustrated in Fig. 1a (see Supplementary Information, Section 2 for the analogous formulation for other kirigami tessellations).

To be able to deploy a kirigami pattern to match a given shape, we also need to ensure that for a given boundary curve ∂S we have a valid deployed configuration. This can be formulated as boundary-shape matching constraints that force all nodes on the boundary of the deployed configuration to lie exactly on ∂S. Mathematically, for every boundary node $\mathbf{p}_i$, this implies that

$$\|\mathbf{p}_i - \widetilde{\mathbf{p}}_i\|^2 = 0 \tag{3}$$

---

[1] John A. Paulson School of Engineering and Applied Sciences, Harvard University, Cambridge, MA, USA. [2] Departments of Physics, and Organismic and Evolutionary Biology, Harvard University, Cambridge, MA, USA. [3] Kavli Institute for Nanobio Science and Technology, Harvard University, Cambridge, MA, USA. *e-mail: lmahadev@g.harvard.edu

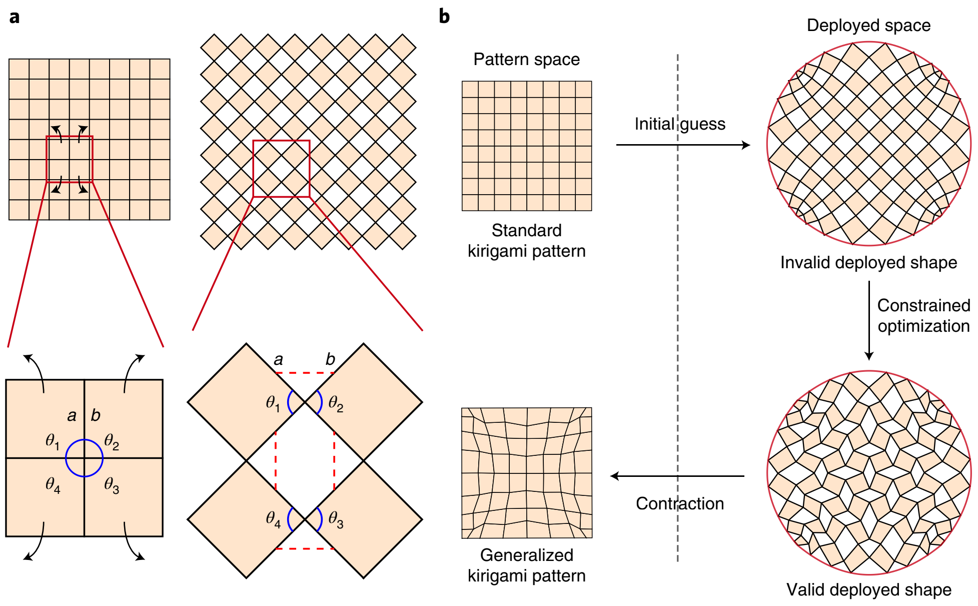

Fig. 1 | Inverse design framework. a, A quad kirigami tessellation and its deployed configuration, with an enlargement of the unit cell of the quad kirigami tessellation and its deployed configuration. Every pair of corresponding edges are connected by a red dashed line. The set of angles corresponding to the same node are highlighted in blue. In a valid deployed configuration of a generalized kirigami pattern, every pair of edges should be equal in length, that is $a=b$, and every set of corresponding angles should add up to 2π, that is, $\theta_1+\theta_2+\theta_3+\theta_4=2\pi$. **b**, Our inverse design framework. Given a standard kirigami tessellation, we start with an initial guess in the deployed space. Here the initial guess shown is a conformal map from the standard deployed configuration to the disc. The initial guess is usually invalid, violating either the edge length constraint or the angle constraint, or not exactly matching the target boundary shape. We then solve a constrained optimization problem to morph the initial guess until it becomes a valid deployed shape, satisfying all constraints. Finally, we use a simple contraction procedure to obtain the generalized kirigami pattern.

where $\widetilde{\mathbf{p}}_i$ is the projection of $\mathbf{p}_i$ onto ∂S and $\|\cdot\|$ is the Euclidean 2-norm. In addition to matching the target boundary shape in the deployed configuration, we can also control the shape of the kirigami tessellations in their undeployed states by introducing boundary angle constraints (see Supplementary Information, Section 2 for details).

While the constraints described above ensure consistency between corresponding edges and angles, they do not prevent the faces from overlapping in the deployed state. To enforce this, we use the following non-overlapping constraint at every angle between two adjacent faces:

$$\langle (\mathbf{b}-\mathbf{a})\times(\mathbf{c}-\mathbf{a}), \hat{\mathbf{n}}\rangle \geq 0 \qquad (4)$$

where $\mathbf{a}$, $\mathbf{b}$ and $\mathbf{c}$ are the nodes of adjacent faces, so that ($\mathbf{b}$, $\mathbf{a}$, $\mathbf{c}$) forms a positive (right-hand ordered) angle between the two faces, and $\hat{\mathbf{n}}=(0,0,1)$ is the outward unit normal.

To find an admissible deployed kirigami structure, we must satisfy the above interior and boundary conditions—this will yield a compact tiling that is related to the deployed state via a non-affine contraction. This can be framed as a constrained optimization problem whose solution is sufficient to guarantee a valid deployed configuration of a generalized kirigami pattern that approximates a prescribed shape. However, without a regularization procedure, the solution is likely to be very rough with large gradients in the shapes of the quads. To produce a smooth kirigami tessellation, we therefore minimize the following objective function:

$$\frac{1}{M}\sum_{i=1}^{M}\left(\sum_{j}\left(\alpha_{i_j}-\beta_{i_j}\right)^2+\sum_{k}\left(a_{i_k}-b_{i_k}\right)^2\right) \qquad (5)$$

where $\alpha_{i_j}, \beta_{i_j}$ are a pair of corresponding angles in two adjacent cells and a_{i_k}, b_{i_k} are the corresponding edge lengths in two adjacent cells, and M is the total number of pairs of adjacent cells, subject to the constraints (1)–(4).

Finally, we need a reasonable first approximation to the given deployed configuration that matches the prescribed boundary curve. This initial condition can be obtained via, for example, a conformal/quasi-conformal map[20,21], although we could use any approximation that preserves the number and connectedness of the quads.

We solve the optimization problem numerically using MATLAB's built-in optimization routine *fmincon* (see Supplementary Information, Section 3), noting that the problem is underconstrained with multiple admissible deployed kirigami patterns (see Supplementary Information, Sections 2 and 4). Once we find a valid deployed structure, we can contract this into its compact pattern form by rotating the faces and thus shrinking the entire structure. We note here that our formulation of the optimization problem shows some algorithmic similarities to our recent study of generalized origami tessellations[22]. This is both natural and inevitable, given the presence of geometrical constraints in both problems as well as a condition of shape matching; indeed, many problems in physical geometry requiring the ability to design shapes subject to constraints will also fall within this framework.

To illustrate the effectiveness of our approach, we first design generalized kirigami patterns to approximately solve an ancient mathematical problem—that of circling the square—and a modern one, making an egg shape from a square. In Fig. 2a, we show that by distorting a periodic kirigami tiling of a square (see Supplementary Information), the deployed configurations can match either a circle or an egg. We can also use this method to generate novel generalized kirigami patterns that, when deployed, approximate different boundary shapes. Figure 2b shows two generalized kirigami patterns; one deployed to approximate a domain with a boundary of mixed curvature, and the other deployed to approximate a rectangle (see Supplementary Information, Section 4 for more generalized

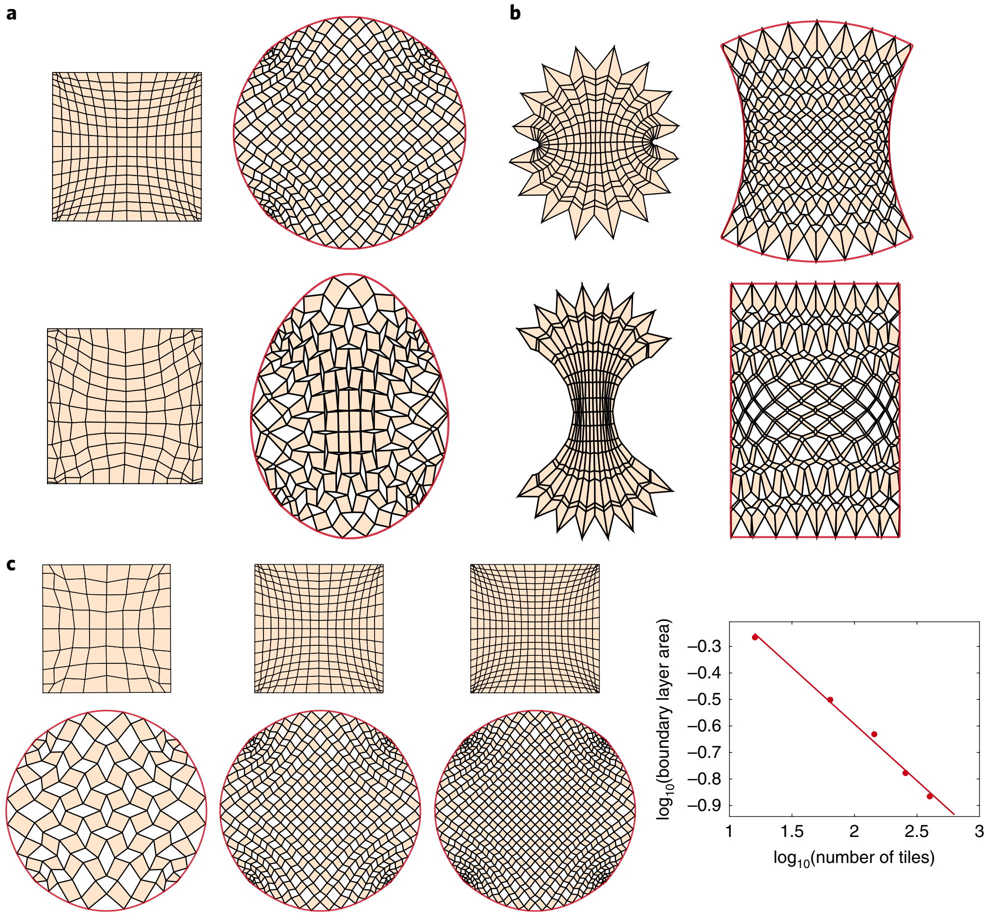

Fig. 2 | Generalized planar kirigami patterns. **a**, Examples of generalized kirigami patterns produced by our method for getting a circle or an egg shape from a square on deployment. **b**, Examples of generalized kirigami patterns produced by our method for achieving boundary shapes with mixed curvature or zero curvature. It can be observed that our method is capable of producing generalized kirigami patterns that match boundary curves with different curvature properties when deployed. **c**, Examples of circling the square with different resolutions (number of tiles = 8 × 8, 16 × 16, 20 × 20), together with a log–log plot of the boundary layer area against the number of tiles. Here, the boundary layer area is defined as the total area of the gaps between the circle and the boundary of the deployed kirigami patterns. The dots on the log–log plot represent kirigami patterns with different numbers of tiles (4 × 4, 8 × 8, 12 × 12, 16 × 16, 20 × 20) and the straight line is the least-square regression line. The result shows that there is an accuracy–effort trade-off in approximating a prescribed shape using generalized kirigami tessellations.

kirigami patterns with other base tessellations). These generalized kirigami patterns with different base tessellations exhibit different behaviours in terms of their effective porosity and overall magnification relative to their compact state (see Supplementary Information, Section 5). These examples naturally raise the question: what are the limits of kirigami design? One expects that these generalized kirigami patterns can only achieve a range of relative area changes, perimeter changes and curvature changes on deployment, and we can provide theorems on these bounds (see Supplementary Information, Section 6). However, since these bounds are a strong function of cut topology, it is possible, nevertheless, to generate a large variety of shapes.

Increasing the accuracy of the approximation using kirigami tessellations can be achieved by using a larger number of smaller tiles, suggesting that there is an accuracy–effort trade-off in matching a prescribed shape. Figure 2c shows several generalized kirigami patterns for circling the square with increasing accuracy; with more tiles, the boundary of the deployed pattern gets closer to a perfect circle (see Supplementary Information, Section 4 for multiresolution results for other patterns). To quantitatively assess the accuracy of the patterns for the approximation, we define the boundary layer area of a generalized kirigami pattern by the total area of the gaps between the target boundary shape and the boundary of the deployed configuration. Figure 2c shows that the boundary layer area (denoted by A) decreases as the number of tiles (denoted by n^2) increases following the power law $A \propto (n^2)^{-1/2} = n^{-1}$. To further explain this, we approximate every boundary gap by a triangle and measure the change in the average triangle base length $\tilde{l}$ and average triangle height $\tilde{h}$ for different resolutions. We observe that $\tilde{l} \propto n^{-1}$ and $\tilde{h} \propto n^{-1}$, and hence the average area of the triangles $\tilde{a} \propto n^{-2}$. As the number of boundary gap triangles is approximately $4n$, we have $A \approx 4n\tilde{a} \propto n^{-1}$.

While our inverse design approach guarantees that the endpoints of deployment, that is the deployed and undeployed states, exist, our method so far is agnostic to the path of deployment. To explore the deployment process of our patterns, we now extend our purely geometrical approach to a mechanical model by having linear springs along the edges and diagonals of the quads, and simple torsional springs at the nodal hinges to model the ligaments there. Then, the total mechanical energy of the system is given by

$$E(\mathbf{x}_1, \mathbf{x}_2, \ldots, \mathbf{x}_N) = \frac{1}{N_s}\sum_{i,j}\left(\frac{\|\mathbf{x}_i - \mathbf{x}_j\| - l_{ij}}{l_{ij}}\right)^2 + \lambda\frac{1}{N_c}\sum_i \theta_i^2 \qquad (6)$$

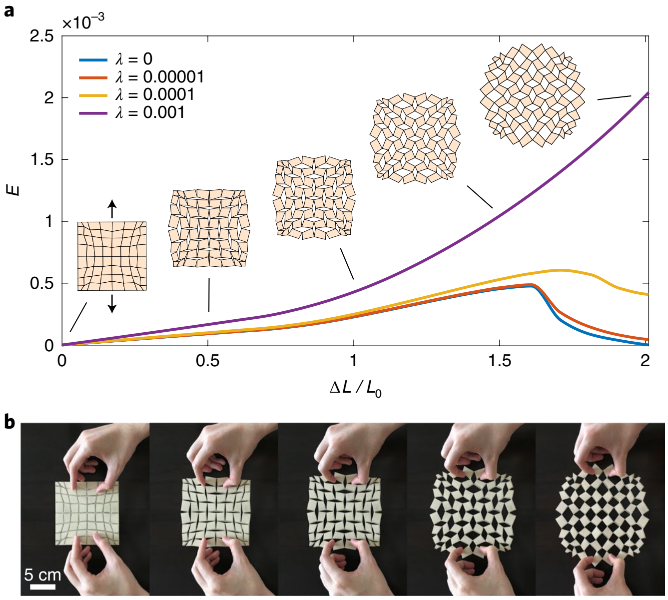

Fig. 3 | Planar deployment of generalized kirigami tessellation. **a**, Energetics of the deployment simulations of the square to circle example with different choice of λ. Here ΔL is the average displacement of the pulling points and L_0 is the average rest length of the extensional springs. The insets show the initial, intermediate and final configurations of the generalized kirigami pattern under deployment. **b**, Snapshots of the deployment of a monostable fabricated model.

where $\mathbf{x}_i$ are the locations of the nodes, θ_i are the angles between every pair of edges created under the cuts, l_{ij} are the rest lengths of the extensional springs, N_s is the total number of extensional springs, N_c is the total number of torsional springs and λ is the ratio of the torsional spring constant to the extensional spring constant. A larger λ corresponds to a thicker ligament, which has a stronger tendency to close up. By iteratively moving the boundary nodes towards the target boundary shape and solving for the intermediate deployed configurations by minimizing (6), we obtain a continuous deployment path. Figure 3a shows the energetics of the deployment simulations as a function of λ: as $\lambda \to 0$, we see the appearance of bistability, while for sufficiently large λ, monostability is observed.

To test our predictions experimentally, we fabricated a physical model by laser cutting a sheet of super-stretchable abrasion-resistant natural rubber. Figure 3b shows the deployment snapshots of a fabricated model with monostability, demonstrating that the simulated path and real deployment have similar behaviours (see Supplementary Information, Section 4 for another fabricated model of a generalized kagome kirigami pattern).

Our inverse design approach has so far focused on approximating planar shapes. However, we now show that it can be extended to fit surfaces in three dimensions as well, so that the undeployed pattern space is in $\mathbb{R}^2$ while the deployed space is in $\mathbb{R}^3$. To fit a surface S in $\mathbb{R}^3$, we replace the boundary shape matching constraints (3) by the surface matching constraints so that every node $\mathbf{x}_i$ in the deployed configuration satisfies the condition

$$\|\mathbf{x}_i - \widetilde{\mathbf{x}}_i\|^2 = 0 \qquad (7)$$

where $\widetilde{\mathbf{x}}_i$ is the projection of $\mathbf{x}_i$ onto S and $\|\cdot\|$ is the Euclidean 2-norm. The extra constraints for controlling the boundary shape of the undeployed configuration in the planar case (analogous to equation (3)) can be directly extended to the surface fitting problem (see Supplementary Information, Section 7).

One can easily note that the contractibility constraints for surface fitting are the same as in equations (1) and (2). For the non-overlapping constraints, to prevent adjacent faces in the deployed configuration from overlapping with or intersecting each other, we replace the unit normal $\hat{\mathbf{n}}$ in equation (4) by the normal computed using one of the two faces. This implies that we must enforce the following inequality constraints for every pair of adjacent faces in the deployed configuration:

$$\langle (\mathbf{b}-\mathbf{a})\times(\mathbf{c}-\mathbf{a}), (\mathbf{c}-\mathbf{a})\times(\mathbf{d}-\mathbf{a})\rangle \geq 0 \qquad (8)$$

where **a**, **b**, **c** and **d** are the nodes of adjacent faces, so that (**b**, **a**, **c**) form a positive (right-hand ordered) angle between the two faces and similarly (**c**, **a**, **d**) also form a positive (right-hand ordered) angle.

In addition to the above constraints, we need to enforce the condition that the faces are planar so that the volume of the tetrahedron associated with each face F vanishes, corresponding to the planarity constraint:

$$\mathrm{Volume}(F) = 0 \qquad (9)$$

More explicitly, for quad tessellations the constraint becomes

$$\langle (\mathbf{b}-\mathbf{a})\times(\mathbf{c}-\mathbf{a}), \mathbf{d}-\mathbf{a}\rangle = 0 \qquad (10)$$

where **a**, **b**, **c** and **d** are the four points of the quad F (see Supplementary Information for generalizations to other base tessellations). We note that this condition, which is automatically satisfied for planar deployment, differentiates the three-dimensional deployment problem from the two-dimensional one.

Finally, to get smooth solutions, we extend the objective function (5) and the contraction process from our planar design approach to three-dimensional surface fitting. This allows us to determine a valid generalized kirigami pattern that can be deployed to approximate a prescribed surface in three dimensions by solving a constrained optimization problem using *fmincon* in MATLAB, with equations (1), (2) and (7)–(9) to be satisfied.

In Fig. 4 we show several generalized kirigami patterns that can be deployed to fit surfaces of varying complexity, such as those with monotonic positive and negative gauss curvature (Fig. 4a,b). Additionally, just as for planar deployments, we can impose extra boundary angle constraints to produce different pattern design effects such as using rectangular quad patterns that can be deployed to fit either a hyperbolic paraboloid as shown in Fig. 4a or an elliptic paraboloid as shown in Fig. 4b. Our approach also allows us to design surfaces with complex non-monotonic Gauss curvature, for example a periodic patch of an egg-carton shape (Fig. 4c) and a bivariate Gaussian (Fig. 4d). In all these examples, we see that our kirigami algorithm provides locally planar tessellations that approximately tile surfaces in $\mathbb{R}^3$ that have non-zero curvature in general. This suggests that the effective surface curvature of the holes between the piecewise planar tilings must be non-zero. To quantify this, we fit every hole in the deployed configurations of our generalized quad kirigami patterns by a bicubic Bézier surface, and compute the mean curvature and the Gaussian curvature of the interpolant (see Supplementary Information, Section 7 for the details); the rightmost columns in Fig. 4 show that the holes between the planar tilings are indeed curved.

To simulate the physical process of deployment, we extend the planar energetic model into three dimensions, with an additional planarity constraint enforced to ensure that all quads remain planar through the simulations. Figure 5a shows the deployment simulations with the four boundaries of a generalized kirigami pattern pulled towards the target positions for fitting a hyperbolic paraboloid. While the intermediate states are warped, the final

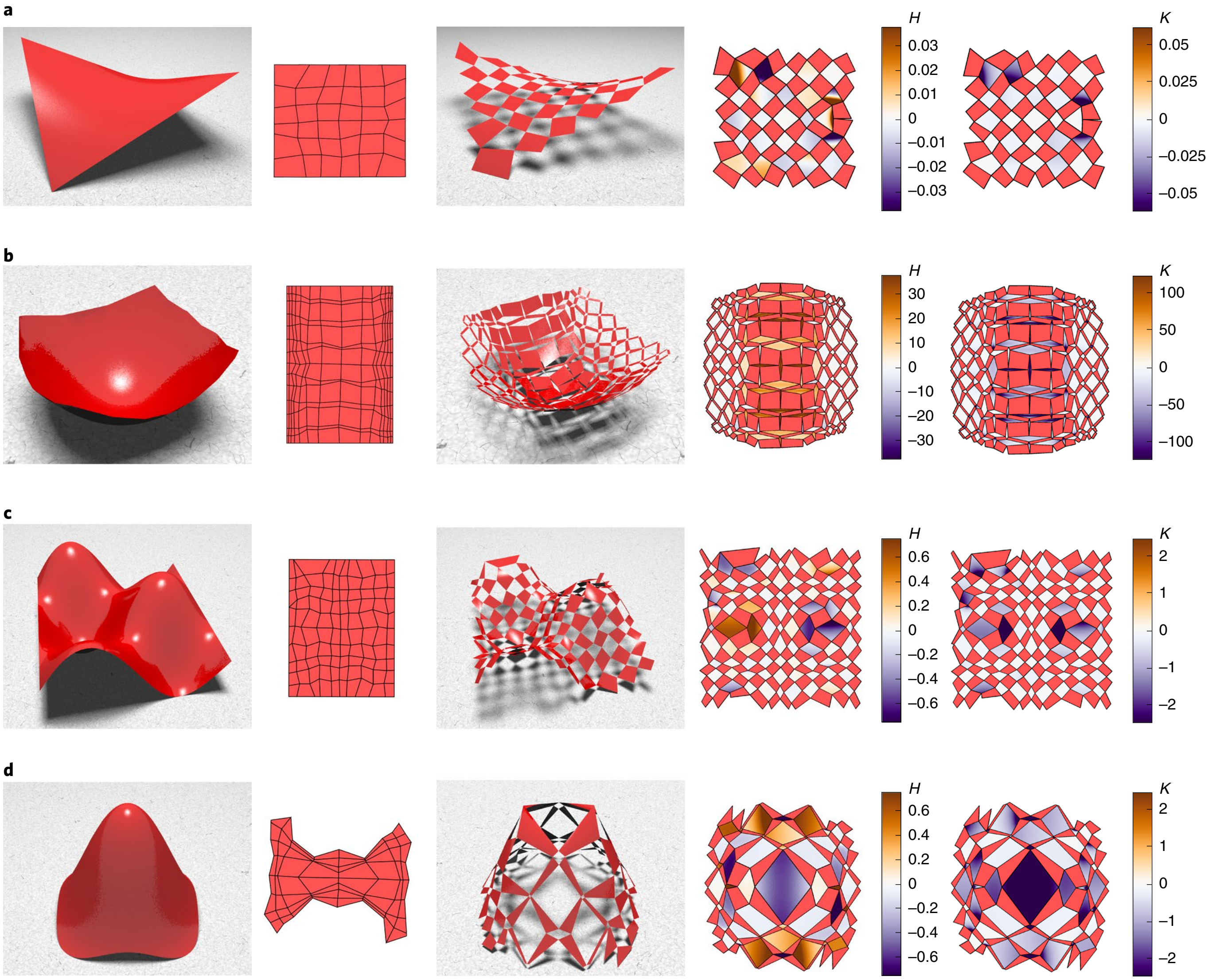

Fig. 4 | Generalized kirigami patterns for three-dimensional surface fitting. a–d, The target surfaces are a hyperbolic paraboloid (with negative curvature) (**a**), a paraboloid (with positive curvature) (**b**), a periodic patch of an egg-carton shape (**c**) and a bivariate Gaussian (**d**). Columns: the target surfaces (leftmost), the generalized kirigami patterns, the deployed configurations of the patterns that fit the target surfaces, the top views of the deployed patterns with the holes coloured with the approximated mean curvature H and the top views of the deployed patterns with the holes coloured with the approximated Gauss curvature K (rightmost).

deployed configuration resembles the shape of a smooth hyperbolic paraboloid very well. Furthermore, just as planar deployment can be either bistable or monostable depending on the value of the torsional spring constant λ, we see the same effect in three-dimensional deployment as well; when λ is large enough, the deployment becomes monostable.

Our inverse design framework is agnostic to the range of possible deployment trajectories aimed towards the target three-dimensional shape, for example by applying displacements to multiple parts of the boundary, as well as fabrication methods of physical kirigami structures. Figure 5b shows the manual deployment of a physical model of a hyperbolic paraboloid fabricated by laser cutting a natural rubber sheet model. We can also create generalized kirigami patterns by creating a mould into which one can pour a liquid polymer and cross-linking it (see Supplementary Information, Section 7 for a fabricated model produced using polydimethylsiloxane (PDMS) and generalized kagome kirigami patterns for surface fitting obtained by our method).

Our inverse design approach allows us to create non-periodic compact kirigami patterns that when deployed can approximate any given shape in two or three dimensions. Simple fabrication methods using cutting and moulding allow us to verify our designs for a few planar and three-dimensional deployable shapes. When our geometry-based constrained optimization framework is generalized to account for the mechanical response of the tilings and hinges, we see that the response of the generalized kirigami patterns can be tuned to switch between monostability and bistability. Altogether, harnessing the underlying topological and geometrical complexity of kirigami in a constrained optimization framework opens the path for the use of generalized kirigami tesselations as the building blocks of shape-morphing mechanical metamaterials. Simultaneously, the present work on inverse design of kirigami together with our ability to solve the inverse design problem in origami[22] suggests a follow-up question: can we combine origami and kirigami, coupling geometry, topology and mechanics, to create structures that morph from any shape

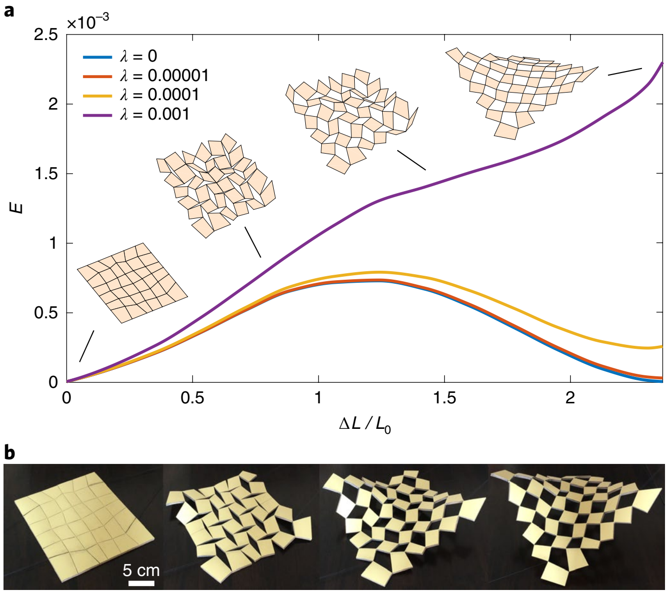

Fig. 5 | Three-dimensional deployment of generalized kirigami tessellation. a, Energetics of the three-dimensional deployment simulations of the pattern in Fig. 4a with different choices of λ. Here ΔL is the average displacement of the pulling points and L_0 is the average rest length of the extensional springs. The insets show the initial, intermediate and final configurations of the pattern under deployment. **b**, Snapshots of the deployment of a monostable fabricated model, with thin threads used for pulling the four sides. Both the numerical simulation and physical deployment results fit the hyperbolic paraboloid very well.

to a given shape with a given mechanical response in two or three dimensions?

Online content

Any methods, additional references, Nature Research reporting summaries, source data, statements of code and data availability and associated accession codes are available at https://doi.org/10.1038/s41563-019-0452-y.

Received: 24 October 2018; Accepted: 4 July 2019;
Published online: 19 August 2019

References

1. Grima, J. N. & Evans, K. E. Auxetic behavior from rotating squares. *J. Mater. Sci. Lett.* **19**, 1563–1565 (2000).
2. Grima, J. N., Alderson, A. & Evans, K. E. Negative Poisson's ratios from rotating rectangles. *Comp. Methods Sci. Technol.* **10**, 137–145 (2004).
3. Grima, J. N., Alderson, A. & Evans, K. E. Auxetic behaviour from rotating rigid units. *Phys. Status Solidi B* **242**, 561–575 (2005).
4. Rafsanjani, A. & Pasini, D. Bistable auxetic mechanical metamaterials inspired by ancient geometric motifs. *Extreme Mech. Lett.* **9**, 291–296 (2016).
5. Sussman, D. M. et al. Algorithmic lattice kirigami: a route to pluripotent materials. *Proc. Natl Acad. Sci. USA* **112**, 7449–7453 (2013).
6. Blees, M. K. et al. Graphene kirigami. *Nature* **524**, 204–207 (2015).
7. Zhang, Y. et al. A mechanically driven form of Kirigami as a route to 3D mesostructures in micro/nanomembranes. *Proc. Natl Acad. Sci. USA* **112**, 11757–11764 (2015).
8. Shyu, T. C. et al. A kirigami approach to engineering elasticity in nanocomposites through patterned defects. *Nat. Mater.* **14**, 785 (2015).
9. Rafsanjani, A. & Bertoldi, K. Buckling-induced kirigami. *Phys. Rev. Lett.* **118**, 084301 (2017).
10. Konaković, M. et al. Beyond developable: computational design and fabrication with auxetic materials. *ACM Trans. Graph.* **35**, 89 (2016).
11. Tang, Y. & Yin, J. Design of cut unit geometry in hierarchical kirigami-based auxetic metamaterials for high stretchability and compressibility. *Extreme Mech. Lett.* **12**, 77–85 (2017).
12. Gatt, R. et al. Hierarchical auxetic mechanical metamaterials. *Sci. Rep.* **5**, 8395 (2015).
13. Kolken, H. M. & Zadpoor, A. A. Auxetic mechanical metamaterials. *RSC Adv.* **7**, 5111–5129 (2017).
14. Mitschke, H., Robins, V., Mecke, K. & Schröder-Turk, G. E. Finite auxetic deformations of plane tessellations. *Proc. R. Soc. Lond. A* **469**, 20120465 (2013).
15. Shan, S., Kang, S. H., Zhao, Z., Fang, L. & Bertoldi, K. Design of planar isotropic negative Poissons ratio structures. *Extreme Mech. Lett.* **4**, 96–102 (2015).
16. Isobe, M. & Okumura, K. Initial rigid response and softening transition of highly stretchable kirigami sheet materials. *Sci. Rep.* **6**, 24758 (2016).
17. Neville, R. M., Scarpa, F. & Pirrera, A. Shape morphing kirigami mechanical metamaterials. *Sci. Rep.* **6**, 31067 (2016).
18. Celli, P. et al. Shape-morphing architected sheets with non-periodic cut patterns. *Soft Matter* **14**, 9744–9749 (2018).
19. Grünbaum, B. & Shephard, G. C. *Tilings and Patterns* (Freeman, 1987).
20. Choi, G. P.-T. & Lui, L. M. A linear formulation for disk conformal parameterization of simply-connected open surfaces. *Adv. Comput. Math.* **44**, 87–114 (2018).
21. Meng, T. W., Choi, G. P.-T. & Lui, L. M. TEMPO: feature-endowed Teichmüller extremal mappings of point clouds. *SIAM J. Imaging Sci.* **9**, 1922–1962 (2016).
22. Dudte, L. H., Vouga, E., Tachi, T. & Mahadevan, L. Programming curvature using origami tessellations. *Nat. Mater.* **15**, 583–588 (2016).

Acknowledgements

This work was supported in part by the Croucher Foundation (G.P.T.C.), National Science Foundation grant no. DMR 14-20570 (L.M.), DMREF grant no. 15-33985 (L.M.) and EFRI grant no. 18-30901 (L.M.). We thank M. Goldberg for contributing to preliminary numerical work, M. Gazzola for helpful initial discussions, and A. Nagarkar and the Whitesides Group for help with fabrication of some of the models using PDMS.

Author contributions

L.H.D. and L.M. conceived the research. G.P.T.C., L.H.D. and L.M designed the research. G.P.T.C. and L.H.D. conducted the simulations and built the models. G.P.T.C., L.H.D. and L.M. analysed the results and wrote the manuscript.

Competing interests

We have filed a patent on our algorithms for kirigami design.

Additional information

Supplementary information is available for this paper at https://doi.org/10.1038/s41563-019-0452-y.

Reprints and permissions information is available at www.nature.com/reprints.

Correspondence and requests for materials should be addressed to L.M.

Methods

Experiment. The physical models shown in Figs. 3 and 5 were fabricated by perforating patterns on super-stretchable abrasion-resistant natural rubber sheets with a laser cutter. See Supplementary Information for further details and another physical model fabricated using PDMS.

Numerical computations. The numerical computations (solving the constrained optimization problem and analysing energetics) were conducted with custom MATLAB code. Analytic gradients of the constraints and objective functions are provided to the *fmincon* constrained optimization routine within the MATLAB environment. See Supplementary Information for further details on the constraints, objective functions and initial conditions.

Data availability

The data that support the findings of this study are available from the corresponding author on reasonable request.

Code availability

Computer codes used in this study are available from the corresponding author on request.

nature materials

SUPPLEMENTARY INFORMATION
https://doi.org/10.1038/s41563-019-0452-y

In the format provided by the authors and unedited.

Programming shape using kirigami tessellations

Gary P. T. Choi[1], Levi H. Dudte[1] and L. Mahadevan[1,2,3]*

---

[1]John A. Paulson School of Engineering and Applied Sciences, Harvard University, Cambridge, MA, USA. [2]Departments of Physics, and Organismic and Evolutionary Biology, Harvard University, Cambridge, MA, USA. [3]Kavli Institute for Nanobio Science and Technology, Harvard University, Cambridge, MA, USA. *e-mail: lmahadev@g.harvard.edu

Supplementary information for
“Programming shape using kirigami tessellations”

Gary P. T. Choi, Levi H. Dudte, L. Mahadevan

Contents

1 Deployable planar tessellations

In the main text we focused on generalized kirigami patterns derived from the quad kirigami tessellations. Here, we consider a wider range of deployable planar tessellations.

It is well known that the only regular polygons that can tile the plane are triangle, square and hexagon. In fact, all of them can be used to produce deployable planar tessellations, such that the deployed configurations of them also tile the plane.

The triangle kirigami tessellation, also known as the kagome tessellation, is a floppy auxetic pattern with six triangles surrounding a single node. As shown in Figure S1**a**, by introducing cuts along the six edges incident to every interior node, we can make the triangle tessellation deployable.

As introduced in the main text, the quad kirigami tessellation is a four-fold auxetic pattern with four quads surrounding a single node. As shown in Figure S1**b**, by introducing cuts along the four edges incident to every interior node, we can make the quad tessellation deployable.

The design of a deployable hexagon tessellation is slightly different. While hexagons can tile the plane, it is impossible to simply introduce cuts along their edges to form a deployable pattern. The reason is that all interior nodes of a regular hexagonal tiling are of degree 3, and hence no matter how cuts are introduced along the three edges incident to a node, the faces will either become fully disconnected or not deployable. One way to design a deployable hexagon tessellation is to leave one hexagonal hole surrounded by six regular hexagonal faces. With the introduction of such holes, it becomes possible for us to introduce cuts along the edges alternatively to get a deployable hexagon tessellation, as illustrated in Figure S1**c**.

Besides the deployable tessellations based on regular polygons, we can also generalize more complex multiple-cell deployable tessellations using our approach. We consider two multiple-cell kirigami patterns derived from Islamic decorative tilings [1], as shown in Figure S1**d**,**e**. Both patterns have unique, singular deployed configurations.

To simplify the computation, we only consider kirigami tessellations which are rectangular. In other words, the tessellations are formed by duplicating one of the unit cells shown in Figure S1 by $m \times n$ times, where m is the number of duplications along the horizontal direction and n is the number of duplications along the vertical direction.

2 Constrained optimization in the deployed space

Denote the fully deployed configuration of a standard kirigami pattern by $\mathcal{D}$, and the target boundary shape together with its interior by $\mathcal{S}$. Our inverse design approach produces a generalized kirigami pattern that approximates ∂S upon deployment by suitably deforming $\mathcal{D}$, and the key step is to solve a constrained optimization problem. In the main text, we discussed the formulation of the constrained optimization problem with a focus on the quad kirigami pattern. Here, we discuss the formulations with the other base patterns that we mentioned above.

Note that the objective function, the boundary shape matching constraints and the non-overlap constraints are the same for all base tessellations. Readers are referred to the main text for a description of them. Below, we focus on the contractibility constraints and the extra constraints.

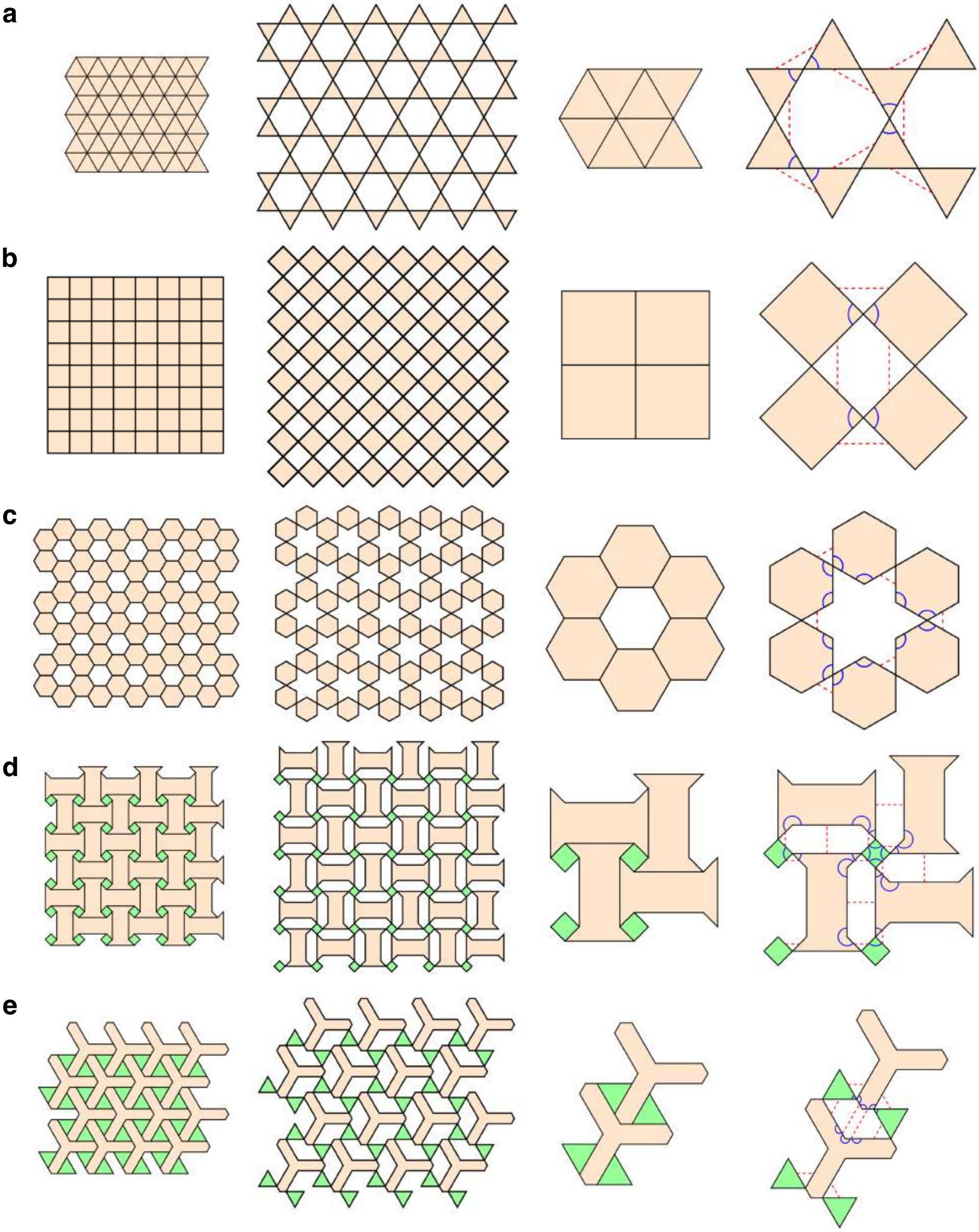

Figure S1: **Five deployable patterns that we consider.** **a**, A triangle kirigami tessellation. **b**, A quad kirigami tessellation. **c**, A hexagon kirigami tessellation. **d**,**e**, Two multiple-cell Islamic kirigami tessellations. Corresponding edge pairs are connected by red dotted lines, and angles involved in the angle constraints are highlighted in blue.

2.1 Contractibility constraints for different generalized kirigami patterns

2.1.1 Generalized kirigami patterns derived from planar tessellations without holes

For the generalized triangle and multiple-cell Islamic kirigami patterns, the contractibility constraints are the same as the ones for the quad pattern. More specifically, for a valid deployed configuration of a generalized kirigami pattern derived from such tessellations, the following two *contractibility* constraints should be satisfied in the deployed space:

(i) *Edge length* constraints: For every pair of edges with edge lengths a, b in the deployed space that correspond to the same cut, we should have

$$a^2 - b^2 = 0. \tag{S1}$$

The edge pairs are connected by red dotted lines in Figure S1.

(ii) *Angle sum* constraints: For every set of angles in the deployed space that correspond to an interior node, their sum should be 2π:

$$\sum_i \theta_i = 2\pi, \tag{S2}$$

where θ_i are angles in the deployed space highlighted in blue in Figure S1.

2.1.2 Generalized kirigami patterns derived from planar tessellations with holes

For generalized kirigami patterns derived from base patterns with holes, such as the hexagon kirigami pattern in Figure S1**c**, the contractibility constraints are slightly different. For the hexagon kirigami pattern, we have the following contractibility constraints:

(i) *Edge length* constraints: For every pair of edges with length a, b in the deployed space that correspond to the same cut, we should have

$$a^2 - b^2 = 0. \tag{S3}$$

The edge pairs are connected by red dotted lines in Figure S1**c**.

(ii) *One-ring angle sum* constraints: For the hexagon kirigami pattern, every hexagonal hole is surrounded by six hexagons. As the angle sum of an n-sided polygon is $(n-2)\pi$, the six angles of the hexagonal hole should add up to 4π. Note that the explementary angles of them can be expressed using the twelve angles in the hexagonal one-ring highlighted in blue in Figure S1**c**. Therefore, in a valid deployed configuration of a generalized hexagon kirigami pattern, we should have

$$6 \times 2\pi - \sum_{i=1}^{12} \theta_i = 4\pi \Leftrightarrow \sum_{i=1}^{12} \theta_i = 8\pi, \tag{S4}$$

where θ_i are the angles in the deployed space highlighted in blue in Figure S1**c**.

(iii) *Diagonal consistency* constraints: The ring angle sum constraints are insufficient to guarantee that the one-ring hexagonal faces form a closed loop, as there is no control on the edge lengths of the hexagonal holes. To ensure the closed loop condition, we impose the diagonal consistency constraints which involve the edge lengths of the hexagonal holes. As depicted in Figure S2, at every hole enclosed by six hexagonal faces, we should have

$$\begin{cases} d_1^2 - d_2^2 = 0, \\ d_3^2 - d_4^2 = 0, \\ d_5^2 - d_6^2 = 0, \end{cases} \tag{S5}$$

where each pair $\{d_1, d_2\}$, $\{d_3, d_4\}$, $\{d_5, d_6\}$ refers to a diagonal of the hole calculated in two ways. More explicitly, we have

$$d_i^2 = \left(a_i - \tfrac{b_i \sin \nu_i}{\sin(\mu_i + \nu_i)}\right)^2 + \left(c_i - \tfrac{c_i \sin \mu_i}{\sin(\mu_i + \nu_i)}\right)^2 + 2\left(a_i - \tfrac{b_i \sin \nu_i}{\sin(\mu_i + \nu_i)}\right)\left(c_i - \tfrac{c_i \sin \mu_i}{\sin(\mu_i + \nu_i)}\right)\cos(\mu_i + \nu_i), \tag{S6}$$

where

$$\mu_i = 2\pi - \gamma_i - \eta_i \tag{S7}$$

and

$$\nu_i = 2\pi - \phi_i - \psi_i. \tag{S8}$$

Note that all the edge lengths a_i, b_i, c_i and the angles $\gamma_i, \eta_i, \phi_i, \psi_i$ are information in the deployed space. Therefore, the diagonal consistency constraints can be imposed in our constrained optimization problem, which takes place in the deployed space.

While the above constraints are discussed in the setting of hexagon kirigami patterns, similar constraints can be established for other kirigami patterns with holes.

2.2 Extra constraints for achieving different effects

Besides the boundary shape matching constraints, the contractibility constraints and the non-overlap constraints, we can impose extra constraints to further control the shape of the generalize kirigami patterns. Below, we discuss a number of possible extra constraints for each tessellation, which lead to different interesting effects on the resulting generalized kirigami patterns.

2.2.1 Regular boundary angle sum constraints for generalized kagome kirigami patterns

We consider enforcing the generalized kagome patterns to be a rectangle up to a small zig-zag effect on the left and the right boundaries, at which the angle sum is desired to be a multiple of $\pi/3$. To achieve this, we impose the following *regular boundary angle sum* constraints. For each boundary node, we denote the number of faces adjacent to it by k and the angles by $\zeta_1, \zeta_2, \ldots, \zeta_k$. We enforce

$$\sum_{i=1}^{k} \zeta_i = \frac{k\pi}{3}. \tag{S9}$$

In other words, the angle sum at the top and the bottom boundary nodes is π, and the angle sum at the left and the right boundary nodes is either $2\pi/3$ or $4\pi/3$. The two corner nodes on the left will have angle sum $2\pi/3$, and the two corner nodes on the right will have angle $\pi/3$.

2.2.2 Rectangular and square boundary constraints for generalized quad kirigami patterns

As mentioned in the main text, we can enforce the boundary of the generalized quad kirigami pattern to be either a rectangle or even a square. To achieve this, we impose the following extra constraints:

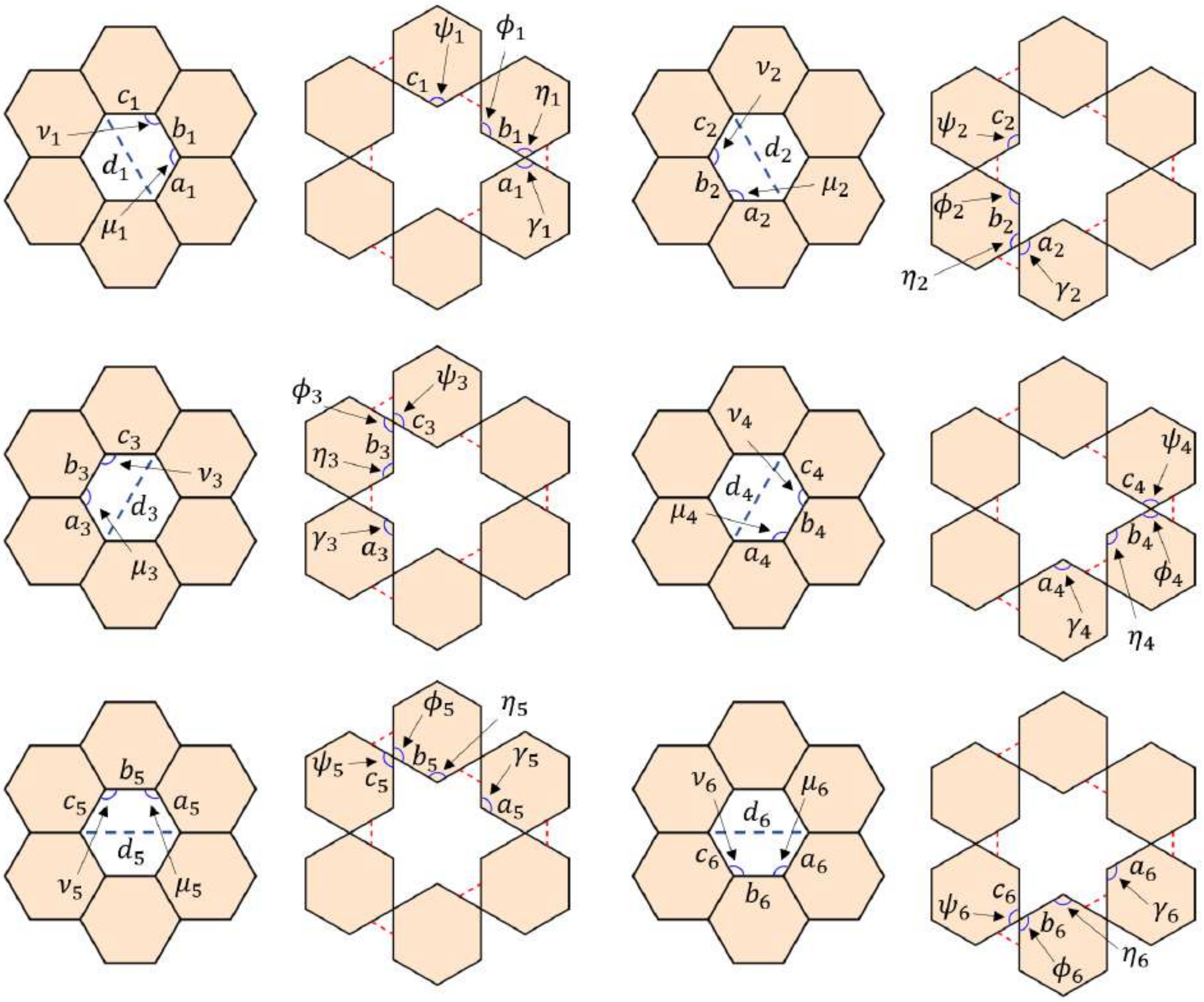

Figure S2: **An illustration of the diagonal consistency constraints for the generalized hexagon kirigami patterns.** Each row shows how the length of a diagonal of the hexagonal hole can be calculated in two ways using the angles and edge lengths in the deployed space.

(i) *Boundary angle* constraints: For every set of two angles ζ_1, ζ_2 in the deployed configuration that correspond to the same boundary node in the kirigami pattern, we enforce

$$\zeta_1 + \zeta_2 = \pi. \tag{S10}$$

For the four angles ξ_1, ξ_2, ξ_3, ξ_4 in the deployed configuration that correspond to four corner angles in the kirigami pattern, we enforce

$$\xi_1 = \xi_2 = \xi_3 = \xi_4 = \frac{\pi}{2}. \tag{S11}$$

These constraints ensure that the deployed configuration corresponds to a rectangular generalized kirigami pattern.

(ii) *Equal boundary length* constraints: On top of the above constraints, we can further enforce the width and the height of the generalized kirigami pattern to be equal in length, making a square generalized kirigami pattern. To achieve this, denote the edges in the deployed configuration which correspond to the top boundary edges in the kirigami pattern by $\vec{e}_{T_i}$, $i = 1, \ldots, m$, and those in the deployed configuration which correspond to the right boundary edges in the kirigami pattern by $\vec{e}_{R_j}$, $j = 1, \ldots, n$. We enforce

$$\|\vec{e}_{T_1}\| + \|\vec{e}_{T_2}\| + \cdots + \|\vec{e}_{T_m}\| = \|\vec{e}_{R_1}\| + \|\vec{e}_{R_2}\| + \cdots + \|\vec{e}_{R_n}\|. \tag{S12}$$

2.2.3 Regular angle constraints for generalized hexagon kirigami patterns

For the generalized hexgaon kirigami patterns, we consider further regularizing their shapes by enforcing the following *regular angle* constraints. For each angle θ in the deployed configuration, we enforce

$$\theta = \frac{2\pi}{3}. \tag{S13}$$

Note that the choice of $2\pi/3$ is compatible with the one-ring angle sum constraints (S4). Even with such restrictions on all angles, we are able to obtain generalized hexagon kirigami patterns that match different shapes upon deployment.

2.2.4 Regular shape constraints for generalized multiple-cell Islamic kirigami patterns

Because of the more complicated geometry of the faces in the multiple-cell Islamic patterns, we impose a few extra constraints to regularize the shape of the generalized kirigami patterns produced.

(i) *Non-self-intersecting* constraints: Unlike the triangle, quad and hexagon patterns, the two multiple-cell Islamic patterns involve polygonal faces which are thinner and with a larger number of sides. To avoid those faces from having self-intersection, we can enforce inequality constraints similar to the non-overlap constraints introduced in the main text. In this case, we use the nodes on such faces to form vectors and enforce that the cross product is consistent with the face normal.

(ii) *Regular angle* constraints:

  (a) For the four-fold Islamic pattern shown in Figure S1**d**, note that it contains four sharp corners for each I-shaped face. To avoid the corners from being squeezed in the generalized four-fold Islamic kirigami patterns, for each of such angles θ in the deployed space we enforce that

$$\theta = \frac{\pi}{4}. \tag{S14}$$

  (b) For the hex Islamic pattern shown in Figure S1**e**, we note that each of the longer sides consists of three nodes, which form an angle of π. To preserve this feature in the generalized hex Islamic kirigami pattern, we enforce that all such straight lines in the deployed configuration of the generalized patterns remain to be straight lines, i.e. the angle sum equals π. Also, note that for this pattern there is no control on the boundary angles. To regularize them, we enforce that all the boundary angles remain unchanged in the deployed configuration of the generalized patterns.

2.3 Initial guess in the deployed space

Note that an initial guess in the deployed space is needed for solving the constrained optimization problem. There are many available options for the initial guess, and below are four choices that we consider in our work.

(i) **Standard deployed configuration**: The standard fully deployed configuration $\mathcal{D}$ of a regular kirigami pattern can be used as an initial guess. Note that it automatically satisfies the contractibility constraints. However, note that the boundary of it is usually very different from the target boundary curve ∂S.

(ii) **Standard deployed configuration with rescaling**: One can also consider suitably rescaling $\mathcal{D}$ according to ∂S so as to reduce the boundary mismatch error. Again, the rescaled configuration satisfies the contractibility constraints, but the boundary mismatch error is still nonzero in general.

(iii) **Conformal map**: We can apply the Schwarz-Christoffel map to produce a non-rigid transformation of $\mathcal{D}$ such that its boundary matches ∂S well. The angles in all faces are also well preserved under the conformal map. However, the edge length mismatch error is large in general.

(iv) **Quasi-conformal map**: We combine recent advances in conformal parameterization [2, 3] to obtain a conformal map $g : \mathcal{S} \to \mathcal{R}$ from $\mathcal{S}$ to a rectangle $\mathcal{R}$, and consider a rescaling transformation $h : \mathcal{R} \to \mathcal{D}$ to achieve the height and width of $\mathcal{D}$. The map $f = (h \circ g)^{-1} : \mathcal{D} \to \mathcal{S}$ is then a quasi-conformal mapping, with $f|_{\partial D} = \partial S$. Because of the rescaling transformation h, all angles will be distorted uniformly under f. Nevertheless, in general the distortion in edge lengths is smaller than that of the conformal map.

2.4 Contraction

To get the generalized kirigami pattern from the deployed configuration, we note that there is a 1-1 correspondence between every face in the pattern space and every face in the deployed space, with each pair of corresponding faces being identical up to translation and rotation. Therefore, we can simply begin from one face, and subsequently rotate and translate the adjacent faces in the deployed configuration to close up the gaps between the edges which correspond to the same cut. After all faces are rotated and translated, we get the generalized kirigami pattern that corresponds to the deployed configuration we obtained in the constrained optimization problem.

3 Implementation

Let $\mathbf{x}_1, \mathbf{x}_2, \dots, \mathbf{x}_N$ be the coordinates of the nodes in the deployed space. The constrained optimization problem with the objective function, the boundary matching constraints, the contractibility constraints and the non-overlap constraints can be solved using `fmincon` in MATLAB, which minimizes the following Lagrangian via gradient descent:

$$\begin{aligned}
&L(\mathbf{x}_1, \mathbf{x}_2, \dots, \mathbf{x}_N, \lambda_{\text{boundary}}, \lambda_{\text{length}}, \lambda_{\text{angle}}, \lambda_{\text{non-overlap}}) \\
=&\frac{1}{M}\sum_{i=1}^{M}\left(\sum_j (\alpha_{i_j} - \beta_{i_j})^2 + \sum_k (a_{i_k} - b_{i_k})^2\right) + \lambda_{\text{boundary}} \sum_i \|\mathbf{p}_i - \widetilde{\mathbf{p}}_i\|^2 \\
&+ \lambda_{\text{length}} \sum (a^2 - b^2) + \lambda_{\text{angle}} \sum \left(\sum \theta_i - 2\pi\right) + \lambda_{\text{non-overlap}} \sum \langle (\mathbf{b} - \mathbf{a}) \times (\mathbf{c} - \mathbf{a}), \vec{n} \rangle.
\end{aligned} \tag{S15}$$

The minimizers $\mathbf{x}_1, \mathbf{x}_2, \dots, \mathbf{x}_N$ then form a valid deployed configuration of a generalized kirigami pattern. In case there are additional constraints to be satisfied, we can also easily include them in the above Lagrangian.

Note that the objective function and all constraints can be expressed solely in terms of the $2N$ coordinates of the nodes $\mathbf{x}_1 = (x_1, y_1), \mathbf{x}_2 = (x_2, y_2), \dots, \mathbf{x}_N = (x_N, y_N)$. To accelerate the computation, we supply the derivatives of the objective function and all constraints using the `SpecifyObjectiveGradient` and `SpecifyConstraintGradient` options in `fmincon`. It is easy to see that all the derivatives have a simple closed form in terms of the $2N$ variables $x_1, \dots, x_N, y_1, \dots, y_N$.

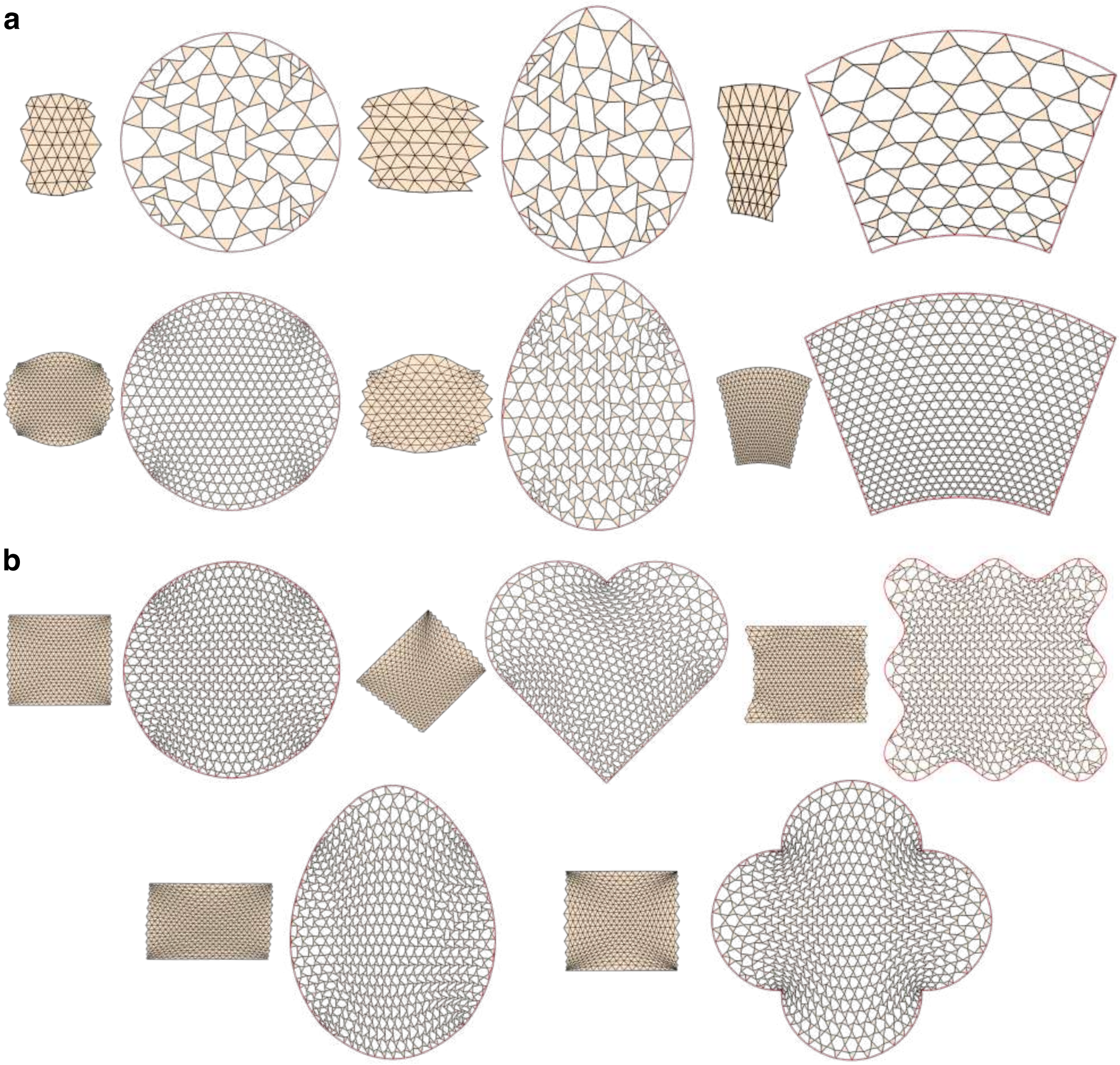

Figure S3: **Generalized kagome kirigami patterns.** **a**, Generalized kagome kirigami patterns with different target boundary shapes and different resolutions obtained by our approach. **b**, The results with the extra regular boundary angle sum constraints described in Section 2.2.1.

4 Results

Figure S3, Figure S4, Figure S5 and Figure S6 show respectively various generalized kirigami patterns obtained by our inverse design approach with the triangle, quad, hexagon and multiple-cell Islamic tessellations. It can be observed that our inverse design approach is capable of producing generalized kirigami patterns that deploy and approximate a wide range of shapes, possibly with different curvature properties or even sharp corners. Besides, the extra constraints that we introduced above can be effectively imposed in the constrained optimization problem to achieve a large variety of additional effects on the shape of the generalized kirigami patterns.

The constrained optimization problem is in general underconstrained and hence different initial guesses can lead to different valid deployed configurations of generalized kirigami patterns. Figure S7 shows the results obtained with four different initial guesses, including the standard deployed configuration of the quad kirigami pattern, the standard deployed configuration with rescaling, a conformal map of the standard deployed configuration and a quasi-conformal map of

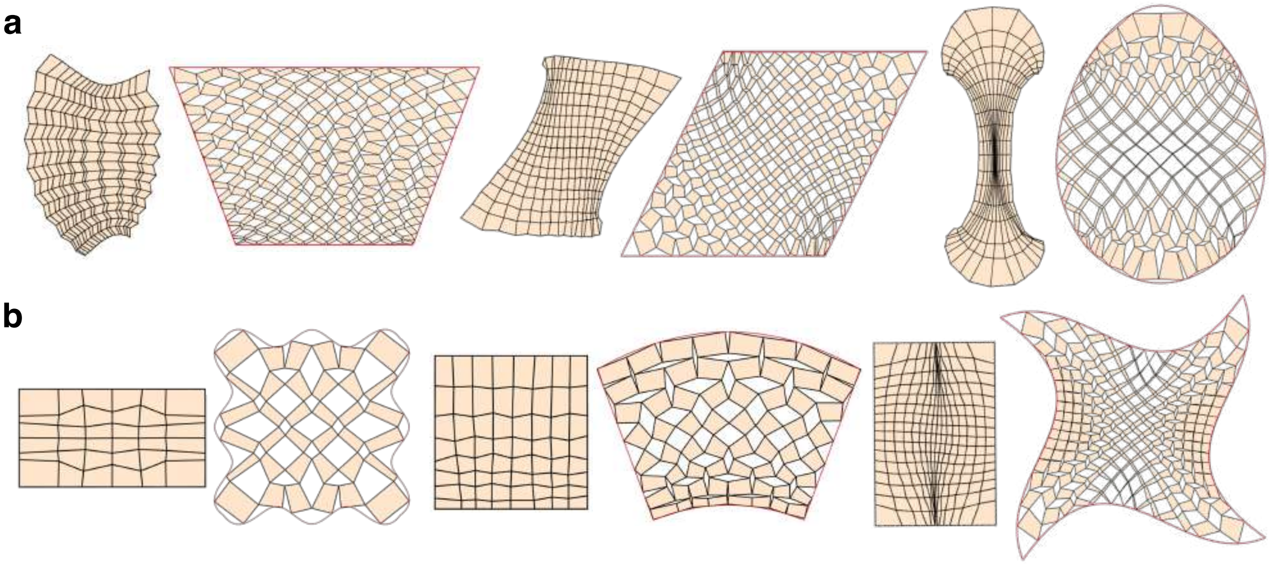

Figure S4: **Generalized quad kirigami patterns.** **a**, Generalized quad kirigami patterns with different target boundary shapes. **b**, The results with the extra constraints enforcing the pattern to be a rectangle or a square as described in Section 2.2.2.

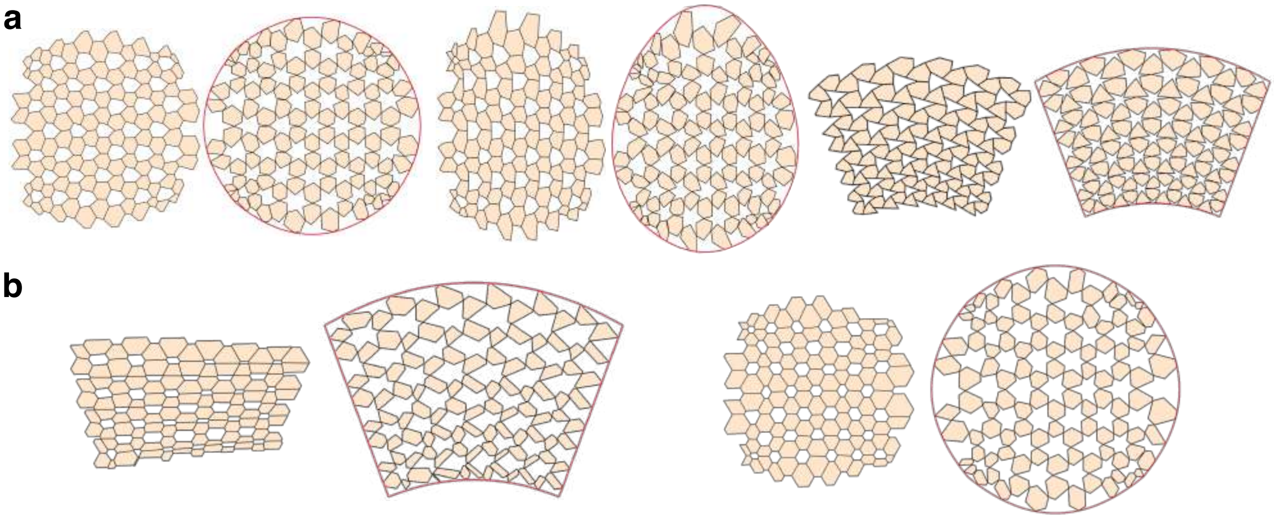

Figure S5: **Generalized hexagon kirigami patterns.** **a**, Generalized hexagon kirigami patterns with different target boundary shapes. **b**, The results with the extra regular angle constraints described in Section 2.2.3.

the standard deployed configuration. Note that all four generalized kirigami patterns obtained by the four initial guesses can be deployed to approximate the same circle, but the patterns and the deployed configurations are all different.

Figure S8 shows a fabricated model of a generalized kagome kirigami pattern obtained by our method for fitting an egg shape, produced by laser cutting a natural rubber sheet. This time, we pin the deployed state of the fabricated model and compare it with the optimization result. It can be observed that the fabrication result resembles the optimization result very well. This demonstrates the effectiveness of our inverse design method.

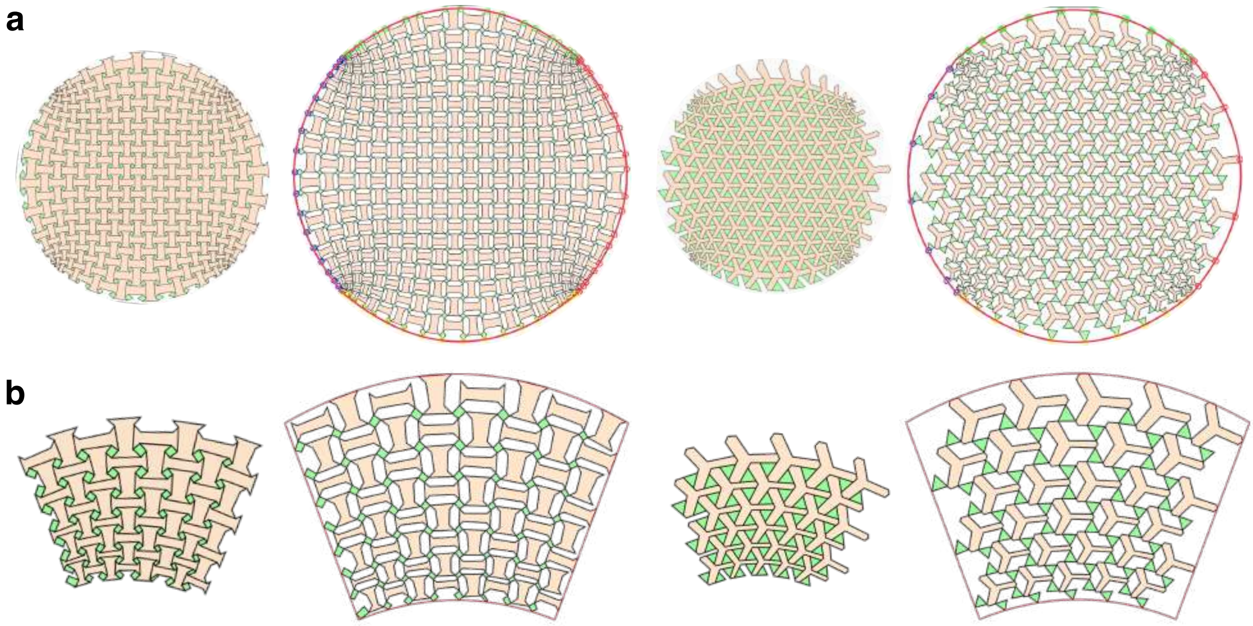

Figure S6: **Generalized multiple-cell Islamic kirigami patterns.** **a**, Generalized multiple-cell Islamic kirigami patterns whose deployed configurations approximate a circle. **b**, The results with the extra regular angle constraints described in Section 2.2.4.

5 Analysis of porosity and magnification factor of generalized kirigami patterns

From the results obtained by our inverse design approach, it can be observed that the generalized kirigami patterns with different types of base tessellations exhibit different properties even if their deployed configurations approximate the same shape. For instance, the size of the generalized kagome kirigami patterns changes significantly upon deployment, while the size of the generalized hexagon kirigami patterns does not change much upon deployment.

To quantitatively analyze their properties, we define the *porosity* of a generalized kirigami pattern by

$$\text{Porosity} = \frac{\text{Area of deployed configuration} - \text{Area covered by material}}{\text{Area of deployed configuration}}. \tag{S16}$$

and the *magnification factor* of a generalized kirigami pattern by

$$\text{Magnification factor} = \frac{\text{Area of deployed configuration}}{\text{Area of contracted configuration}}. \tag{S17}$$

Here, the area of a configuration is defined to be the area of the region enclosed by its boundary nodes, and the area covered by material is defined to be the total area of all faces in a pattern.

Figure S9**a**,**b** show the porosity and magnification factor of the generalized kirigami patterns that deploy and approximate different target shapes. 8 target shapes are considered for each of the triangle, quad and hexagon tessellations. An example of different patterns that deploy to approximate a rainbow shape is shown in Figure S9**c**.

Ideally, for every target shape, the area of the deployed configurations with the triangle, quad and hexagon tessellations should be as close as possible to the area of the target shape. However, it can be observed that the deployed configurations of the generalized hexagon kirigami patterns usually achieve a slightly smaller area when compared to those of the triangle and

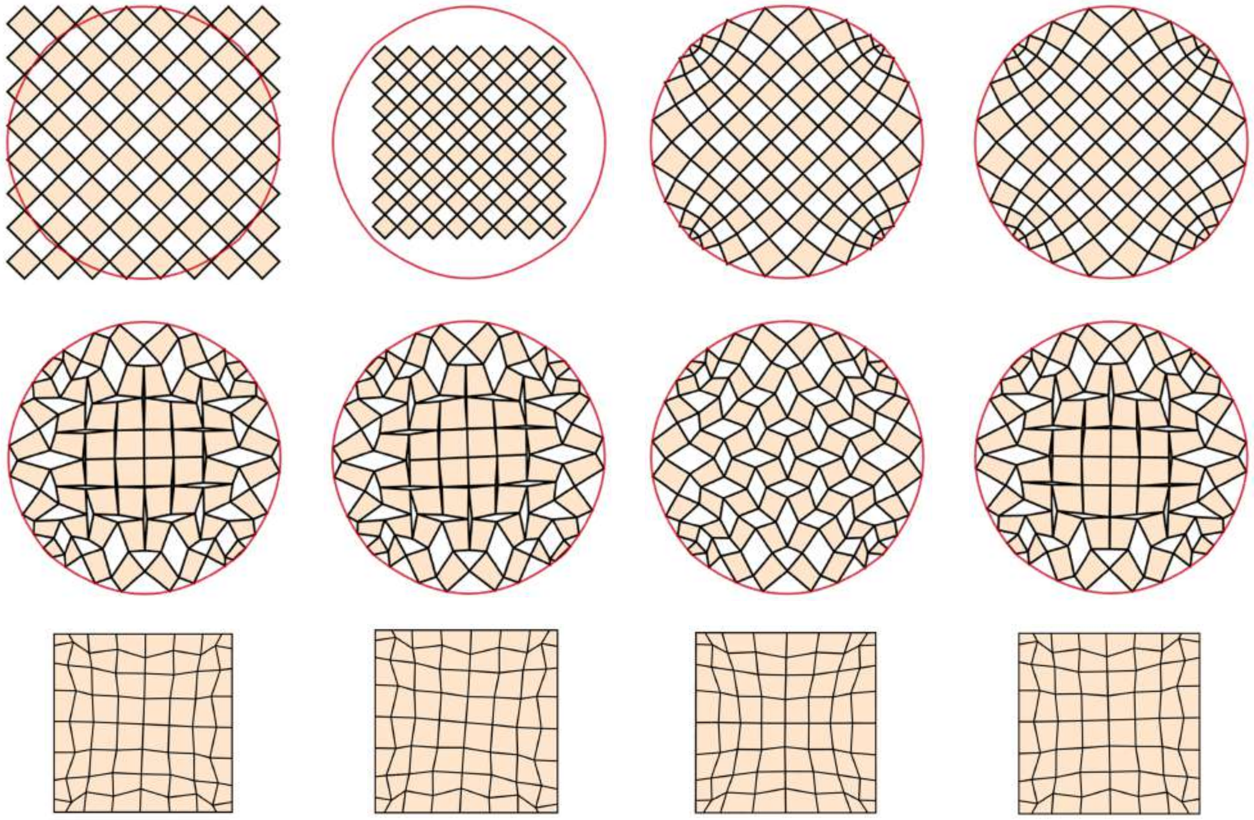

Figure S7: **An example illustrating that the generalized kirigami patterns obtained with different initial guesses can be different.** Each row shows the initial guess, the constrained optimization result, and the generalized kirigami pattern obtained. Left: The standard deployed configuration of the quad kirigami pattern. Middle left: The standard deployed configuration with rescaling. Middle right: Conformal map. Right: Quasi-conformal map.

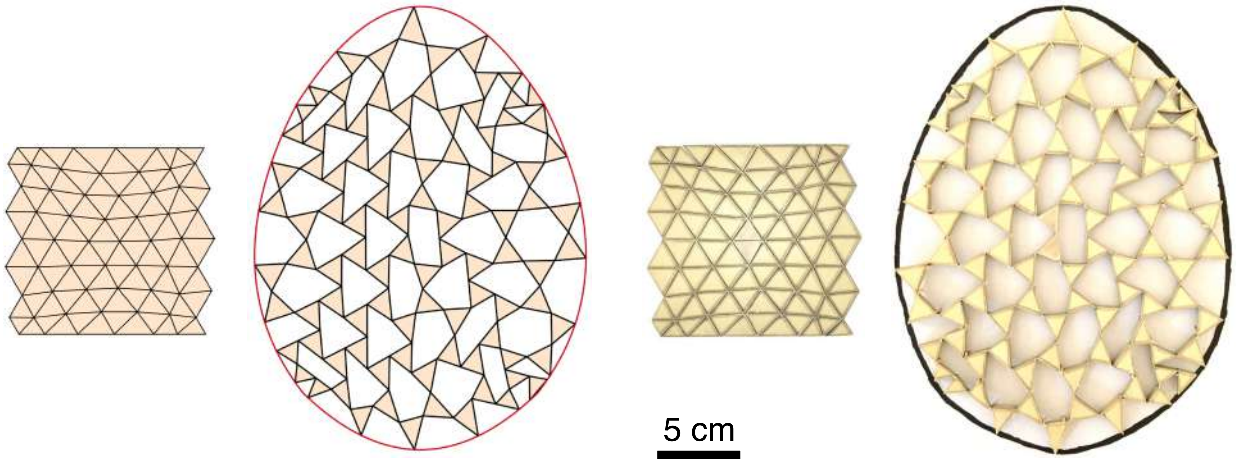

Figure S8: **A generalized kirigami pattern for fitting an egg shape with a fabricated model.** The two figures on the left show the undeployed and deployed configurations of the numerical optimization result obtained by our inverse design method. The two figures on the right show a fabricated model of the pattern and its deployed state. Pins are used to fix the position of the deployed fabricated model.

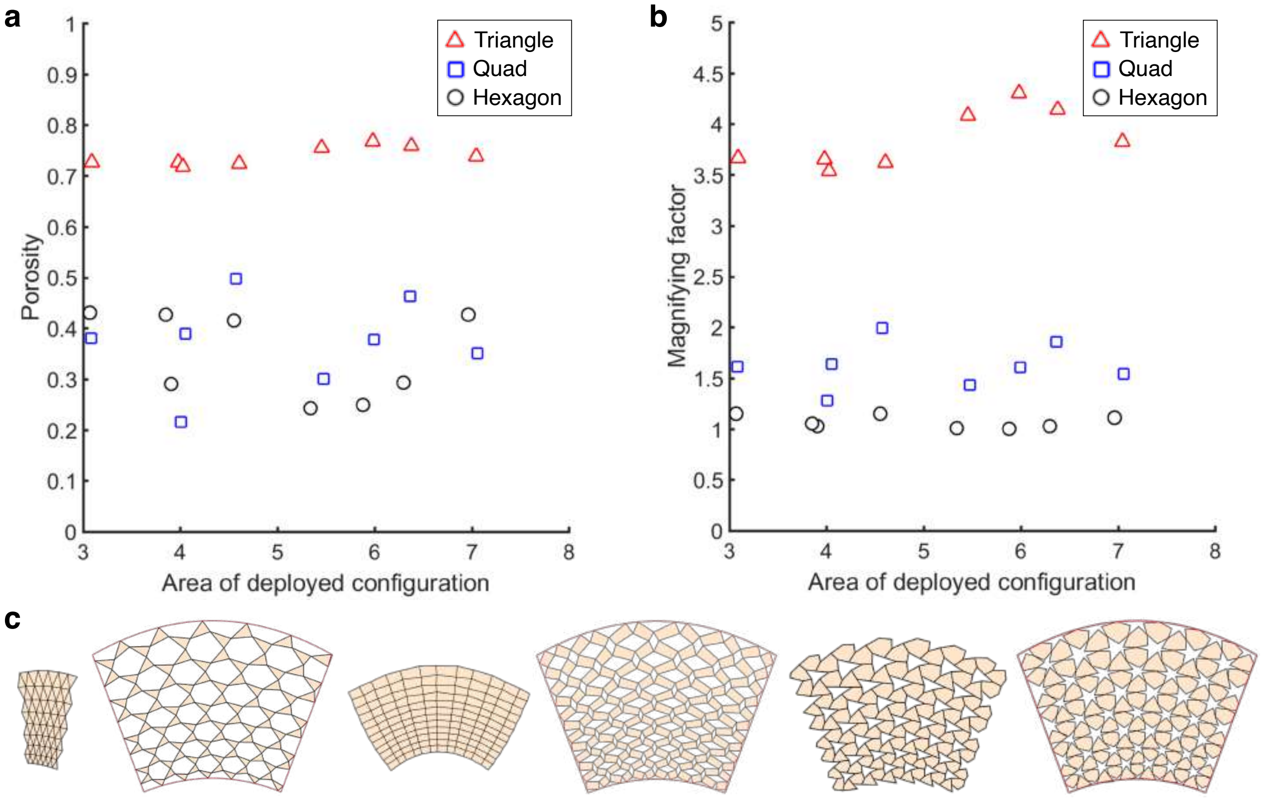

Figure S9: **Porosity and magnification factor of different generalized kirigami patterns**. **a**, The porosity of different generalized kirigami patterns. **b**, The magnification factor of different generalized kirigami patterns. **c**, Examples of the generalized triangle, quad and hexagon kirigami patterns for which the deployed configurations approximate the same boundary shape.

quad patterns. One possible reason is that hexagons are less flexible than triangles and quads in approximating shapes with higher curvature.

From the plot of porosity, it can be observed that the generalized kagome kirigami patterns achieve much higher porosity than the two other types of patterns. The porosity of the generalized quad and hex patterns are similar.

From the plot of magnification factor, it can again be observed that the generalized kagome kirigami patterns achieve much higher magnification factor than the two other types of patterns. Note that the magnification factor for the generalized hexagon patterns is close to 1, which implies that there is only a change in the shape of the hexagonal holes of the generalized hexagon kirigami patterns under deployment, while the entire shape of the patterns does not change much.

The above analysis suggests that the generalized kagome kirigami patterns are well-suited for applications that require a large change in area under deployment in order to save materials. The generalized quad kirigami patterns can be used when it is desired to achieve a moderate area change and porosity upon deployment. The generalized hexagon kirigami patterns are suitable for applications which require a change in the shape of the holes without much change in the overall area upon deployment, such as the design of a filter for allowing particles with a certain shape to pass through.

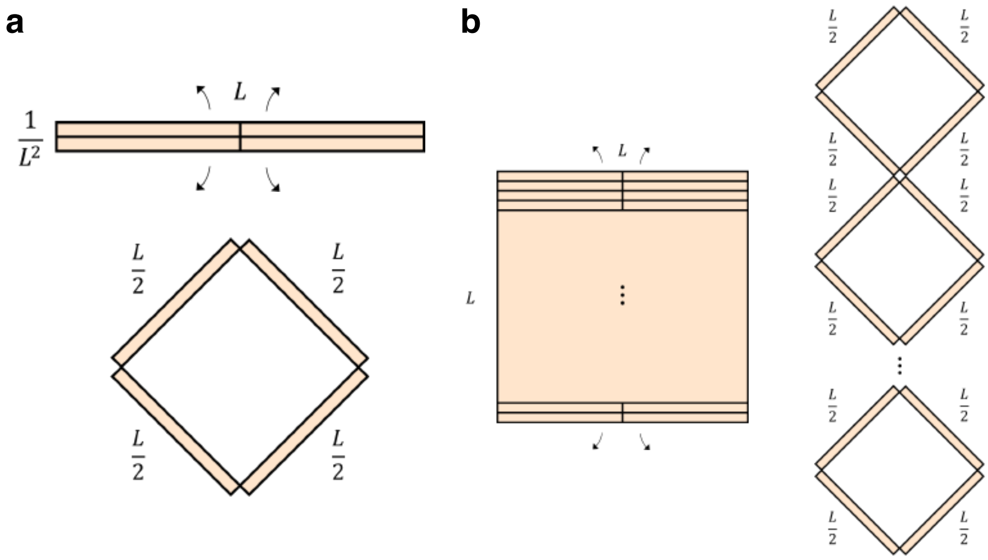

Figure S10: **Two examples of generalized quad kirigami**. **a**, A 2 × 2 generalized quad kirigami with width L and height $1/L^2$. **b**, A $2L^3 \times 2$ generalized quad kirigami formed by L^3 copies of the 2 × 2 kirigami shown in **a**.

6 Theoretical limits of the shape change of generalized kirigami patterns upon deployment

It is natural to ask about the limit of the shape change of a generalized kirigami pattern upon deployment. In this section, we study the limits for the change in area, perimeter and curvature of a planar generalized kirigami pattern upon deployment. To simplify our analysis, we focus on generalized quad kirigami patterns (i.e. the faces are all quadrilateral).

6.1 Area change upon deployment

We first study the area change Δ_{area} of a generalized kirigami pattern upon deployment, i.e.

$$\Delta_{\text{area}} = \frac{\text{Area of the deployed configuration}}{\text{Area of the contracted configuration}} - 1. \tag{S18}$$

6.1.1 Area change is unbounded if either the boundary shape of the contracted configuration or the cut topology is not fixed

We first consider the case that we are given a cut topology of the generalized kirigami (e.g. the resolution is $m \times n$) while there is no condition on the boundary shape of the contracted configuration. In this case, we can show that the area change is unbounded.

Consider a 2×2 generalized quad kirigami with width L and height $1/L^2$ as shown in Figure S10**a**. The area of the contracted configuration is $L \times 1/L^2 = 1/L$. Upon deployment, the increase in area of it is $(L/2) \times (L/2) = L^2/4$. Therefore, the area change is

$$\Delta_{\text{area}} = \frac{L^2/4}{1/L} = \frac{L^3}{4}. \tag{S19}$$

Taking $L \to \infty$, Δ_{area} tends to infinity. This shows that the area change is unbounded.

Analogously, for any other given cut topology, we can follow the construction above and obtain a generalized kirigami that achieves arbitrarily large Δ_{area} upon deployment.

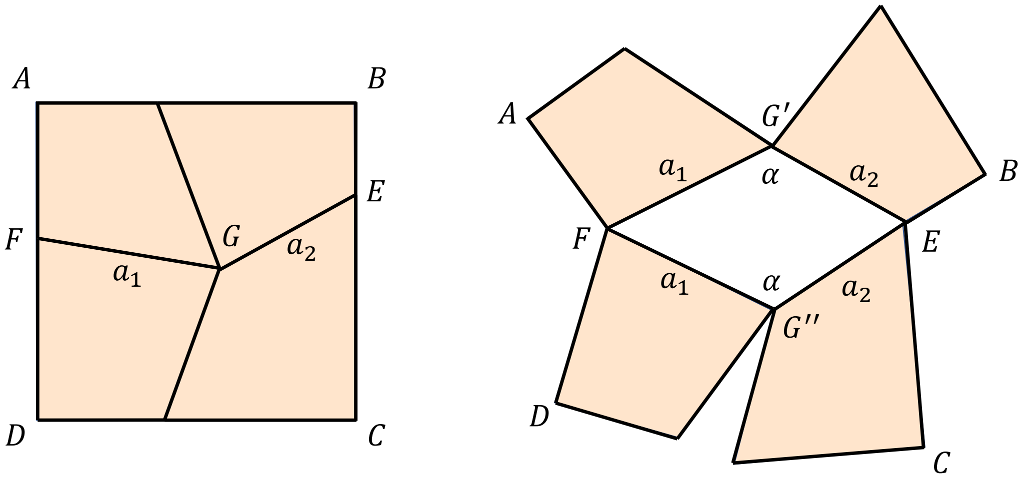

Figure S11: **A** 2×2 **generalized quad kirigami and its deployed configuration.**

Now consider the case that we are given the boundary shape of the contracted configuration while there is no restriction on the number of cuts to be introduced. In this case, we can again show that the area change is unbounded.

Suppose the boundary shape of the contracted configuration is required to be a perfect square with width and height L. Consider a $2L^3 \times 2$ generalized quad kirigami as shown in Figure S10**b**, which consists of L^3 copies of the 2×2 generalized quad kirigami shown in Figure S10**a**. It is easy to see that the width of the pattern is L, and the height is $\frac{1}{L^2} \times L^3 = L$. Upon deployment, each copy leads to an area increase of $L^2/4$. Therefore, we have

$$\Delta_{\text{area}} \geq \frac{(L^2/4) \times L^3}{L^2} = \frac{L^3}{4}. \tag{S20}$$

Taking $L \to \infty$, Δ_{area} also tends to infinity.

Analogously, for any other given boundary shape of the contracted configuration of a generalized kirigami pattern, we can take four points on the boundary of it as the four corners and consider a $2L^3 \times 2$ cut topology. As $L \to \infty$, we can again achieve an arbitrarily large area change upon deployment.

6.1.2 Area change is bounded if both the boundary shape of the contracted configuration and the cut topology are fixed

The analysis above suggests that we can obtain a generalized kirigami pattern that achieves arbitrary area change upon deployment by playing around with either the contracted shape or the cut topology. By contrast, it can be observed that the area change is bounded in case both of them are fixed.

As an illustration, we consider a 2×2 generalized quad kirigami for which the boundary shape of its contracted configuration is a perfect square with unit width and height (see Figure S11.

If the cut pattern is regular (i.e. the 2×2 kirigami shown in Figure S1**b**), then clearly we have

$$\Delta_{\text{area}} = \frac{5}{4} - 1 = \frac{1}{4}. \tag{S21}$$

Now suppose we relax the condition by only requiring the cuts to be vertical or horizontal (i.e. the cut pattern forms four rectangular faces but not necessarily identical squares).

Proposition 1 *For a 2×2 generalized quad kirigami with all cuts being vertical or horizontal, we have*

$$\Delta_{area} \leq \frac{1}{4}, \tag{S22}$$

where the equality holds if and only if the generalized kirigami is regular.

Proof. Using the notation in Figure S11, in this case we have $a_1 + a_2 = 1$. Note that the area of the interior hole in the deployed configuration is $a_1 a_2 \sin\alpha$. By AM-GM inequality,

$$\sqrt{a_1 a_2} \leq \frac{a_1 + a_2}{2} = \frac{1}{2} \Rightarrow a_1 a_2 \leq \frac{1}{4}, \tag{S23}$$

where the equality holds if and only if $a_1 = a_2 = 1/2$. Hence,

$$\Delta_{area} \leq \frac{1}{4} \sin\alpha \leq \frac{1}{4}. \tag{S24}$$

The equality holds if and only if $a_1 = a_2 = 1/2$ and $\alpha = \pi/2$. In other words, the equality holds if and only if the generalized kirigami is regular. ■

The above proposition suggests that among all 2×2 generalized quad kirigami patterns with only vertical and horizontal cuts, the regular one is with the greatest area change upon deployment. In fact, it can be shown that an even greater area change can be achieved if the cuts are not vertical or horizontal, but the area change is still bounded.

Proposition 2 *For a 2×2 generalized quad kirigami, we have*

$$\Delta_{area} < \frac{3}{2}. \tag{S25}$$

Proof. We refer to Figure S11 for the notation of edge lengths and angles. The area of the interior hole in the deployed configuration is given by

$$a_1 a_2 \sin\alpha \leq a_1 a_2 \leq \frac{a_1^2 + a_2^2}{2}, \tag{S26}$$

where the first equality holds if and only if $\alpha = \pi/2$, and the second equality holds if and only if $a_1 = a_2$.

Now, to find the maximum value of $a_1^2 + a_2^2$, we consider the contracted configuration and let $G = (x, y)$, $E = (1, e)$ and $F = (0, f)$. Then

$$\begin{aligned} a_1^2 + a_2^2 &= (x-1)^2 + (y-e)^2 + x^2 + (y-f)^2 \\ &= 2\left(x - \frac{1}{2}\right)^2 + \frac{1}{2} + (y-e)^2 + (y-f)^2. \end{aligned} \tag{S27}$$

Since $x, y, e, f \in [0, 1]$, we have

$$\max a_1^2 + a_2^2 = 2\left(\frac{1}{2}\right)^2 + \frac{1}{2} + 1 + 1 = 3, \tag{S28}$$

where the maximum is attained if and only if $(x, y, e, f) = (0, 1, 0, 0)$, $(0, 0, 1, 1)$, $(1, 1, 0, 0)$ or $(1, 0, 1, 1)$. As the cut pattern that we consider is non-degenerate, none of the four solutions above can be achieved in the contracted configuration. Therefore, we have

$$\Delta_{area} \leq \frac{a_1^2 + a_2^2}{2} < \frac{3}{2}. \tag{S29}$$

■

The above analysis shows that the area change of a 2×2 generalized quad kirigami with prescribed contracted shape upon deployment is always bounded regardless of its cut geometry. Analogously, for any other given cut topology and boundary shape of the contracted configuration, the above approach can be used to prove that the area change upon deployment is bounded.

6.2 Perimeter change upon deployment

We then study the perimeter change of a generalized kirigami pattern upon deployment:

$$\Delta_{\text{perimeter}} = \frac{\text{Perimeter of the deployed configuration}}{\text{Perimeter of the contracted configuration}} - 1. \tag{S30}$$

6.2.1 Perimeter change is unbounded if the cut topology is not fixed

Suppose we are given the boundary shape of the contracted configuration of a generalized kirigami pattern, while there is no restriction on the number of cuts to be introduced. In this case, we can show that the perimeter change is unbounded.

We consider the example shown in Figure S10**b**. For this example, note that the boundary of the deployed configuration consists of $4L^3$ segments with length $\frac{L}{2}$ and $4L^3 + 4$ segments with length $\frac{1}{2L^2}$. Therefore, we have

$$\Delta_{\text{perimeter}} = \frac{4L^3 \cdot \frac{L}{2} + (4L^3 + 4) \cdot \frac{1}{2L^2}}{4L} - 1 = L^3 + \frac{1}{L^3}. \tag{S31}$$

Taking $L \to \infty$, we have $\Delta_{\text{perimeter}} \to \infty$.

Analogous to the study of area change, by suitably modifying the above example, it is easy to see that the perimeter change is unbounded for any given boundary shape of the contracted configuration as long as the cut topology is not fixed.

6.2.2 Perimeter change is bounded if the cut topology is fixed

Now suppose the cut topology of the generalized kirigami pattern is fixed (e.g. the resolution of it is $m \times n$). In this case, we can show that the perimeter change of the generalized kirigami upon deployment is always bounded.

Let p be the perimeter of the contracted configuration of a generalized kirigami. Let d be the diameter of the smallest circle which circumscribes the contracted configuration. It is easy to see that $d \leq p$.

As the resolution is $m \times n$, there are at most $2(m-1) + 2(n-1) = 2m + 2n - 4$ new boundary edges upon deployment, and each of them must be with length not greater than d. Hence, we have

$$\Delta_{\text{perimeter}} \leq \frac{p + (2m + 2n - 4)d}{p} - 1 = \frac{(2m + 2n - 4)d}{p} \leq 2m + 2n - 4. \tag{S32}$$

This shows that the perimeter change is bounded with a fixed cut topology.

6.3 Curvature change upon deployment

Finally, we study the curvature change of generalized kirigami patterns upon deployment. Here, the curvature is defined by smoothly connecting the nodes in the deployed configuration which correspond to the boundary codes in the contracted configuration (i.e. the nodes at the zig-zag parts near the deployed boundary are not taken into account).

6.3.1 Curvature change is unbounded if the cut topology is not fixed

The example shown in Figure S10**b** suggests that a target shape with very highly curved parts can be approximated by a generalized kirigami even if the boundary shape of the contacted configuration is fixed, and hence the curvature change upon deployment is unbounded.

6.3.2 Curvature change is bounded if the cut topology is fixed

It is well known that for any smooth simple closed plane curve C, the total curvature is 2π:

$$\int_C k(s)ds = 2\pi. \tag{S33}$$

For the case that the cut topology is fixed, let C be the boundary of a deployed configuration. We have already shown that the perimeter change is bounded in this case, and hence the length of C is bounded. From the above total curvature formula, the curvature change is also bounded.

7 Generalized kirigami patterns for surface fitting

As discussed in the main text, we can extend our inverse design approach for producing generalized kirigami patterns whose deployed configuration approximate a prescribed surface.

In the main text, we presented an analysis on the curvature at the holes of the deployed configurations of generalized quad kirigami patterns. Here, we describe the technical details of the analysis. Suppose $\mathbf{p}_1, \mathbf{p}_2, \mathbf{p}_3, \mathbf{p}_4$ are the four vertices in anti-clockwise orientation of a hole in the deployed configurations. To study the curvature residing at the hole, we consider fitting the hole by a smooth surface. In particular, the surface should be compatible with all the adjacent quads along the straight edges. A suitable candidate for such surface is the bicubic Bézier surface [4] in the form

$$\mathbf{X}(u,v) = \sum_{i=0}^{3}\sum_{j=0}^{3} B_i^3(u)B_j^3(v)\mathbf{k}_{i,j}, \tag{S34}$$

where $u, v \in [0,1]$. Here, $\mathbf{k}_{i,j}$ are 16 control points including the four vertices $\mathbf{k}_{0,0} = \mathbf{p}_1$, $\mathbf{k}_{3,0} = \mathbf{p}_2$, $\mathbf{k}_{3,3} = \mathbf{p}_3$, $\mathbf{k}_{0,3} = \mathbf{p}_4$, and the remaining control points are

$$\begin{aligned}
\mathbf{k}_{1,0} &= \frac{2\mathbf{k}_{0,0}+\mathbf{k}_{3,0}}{3}, \mathbf{k}_{2,0} = \frac{\mathbf{k}_{0,0}+2\mathbf{k}_{3,0}}{3}, \mathbf{k}_{1,3} = \frac{2\mathbf{k}_{0,3}+\mathbf{k}_{3,3}}{3}, \mathbf{k}_{2,3} = \frac{\mathbf{k}_{0,3}+2\mathbf{k}_{3,3}}{3},\\
\mathbf{k}_{0,1} &= \frac{2\mathbf{k}_{0,0}+\mathbf{k}_{0,3}}{3}, \mathbf{k}_{0,2} = \frac{\mathbf{k}_{0,1}+2\mathbf{k}_{0,3}}{3}, \mathbf{k}_{3,1} = \frac{2\mathbf{k}_{3,0}+\mathbf{k}_{3,3}}{3}, \mathbf{k}_{3,2} = \frac{\mathbf{k}_{3,0}+2\mathbf{k}_{3,3}}{3},\\
\mathbf{k}_{1,1} &= \frac{2\mathbf{k}_{1,0}+\mathbf{k}_{1,3}}{3}, \mathbf{k}_{1,2} = \frac{\mathbf{k}_{1,0}+2\mathbf{k}_{1,3}}{3}, \mathbf{k}_{2,1} = \frac{2\mathbf{k}_{2,0}+\mathbf{k}_{2,3}}{3}, \mathbf{k}_{2,2} = \frac{\mathbf{k}_{2,0}+2\mathbf{k}_{2,3}}{3}.
\end{aligned} \tag{S35}$$

$B_0^3, B_1^3, B_2^3, B_3^3$ are the Bernstein polynomials of degree 3 given by

$$B_i^3(u) = \binom{3}{i} u^i(1-u)^{3-i}. \tag{S36}$$

The boundary of the Bézier surface is given by $\{\mathbf{X}(u,v) : u, v = 0, 1\}$. As there are four collinear control points on each boundary edge of the hole, the Bézier surface will pass through all the edges exactly, making the surface compatible with all the surrounding quads. The surface is planar if and only if the four vertices of the hole are coplanar.

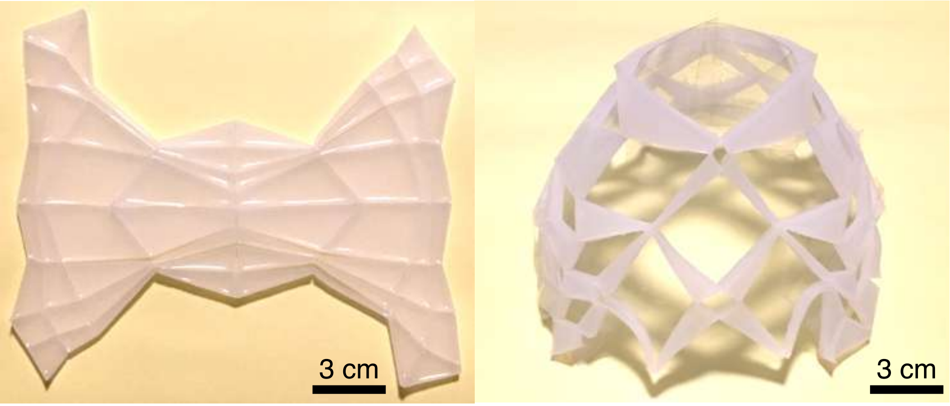

Figure S12: **A physical model of the generalized quad pattern shown in Figure 4d in the main text fabricated using PDMS.** The model achieves a significant shape change and fits a hat-like surface (the underlying transparent sheet) upon deployment.

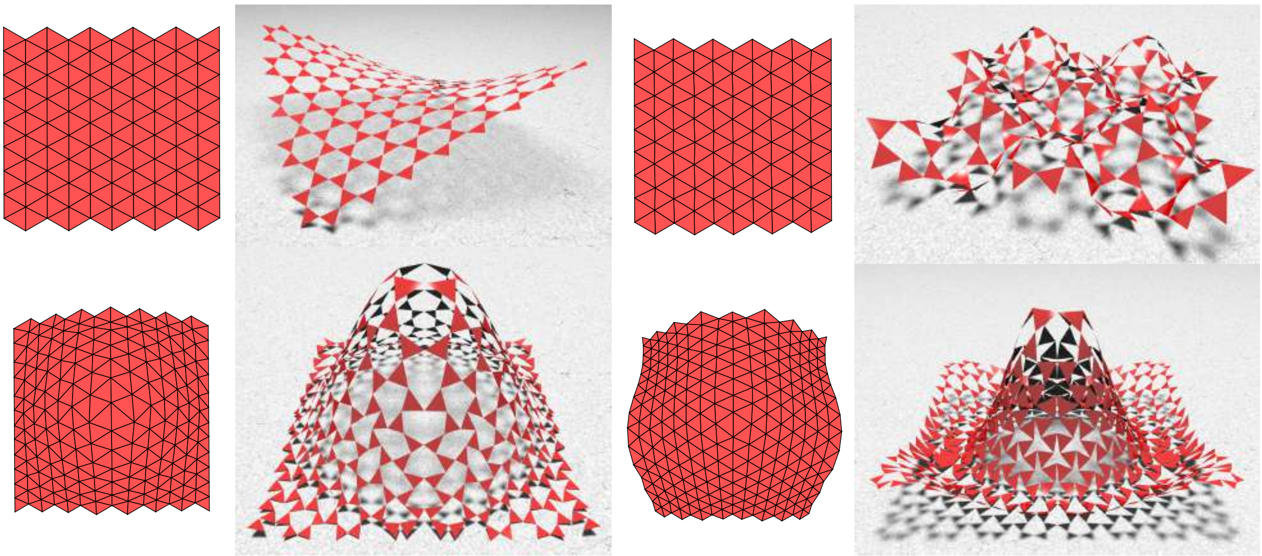

Figure S13: **Generalized kagome kirigami patterns for surface fitting.** The target surfaces are respectively a hyperbolic paraboloid, a landscape surface with multiple peaks, a bivariate Gaussian and a Mexican hat. For each target surface, the resulting generalized kirigami pattern and its deployed configuration are shown. It can be observed that our approach is capable of controlling the boundaries and the shape of the triangular faces of the generalized kirigami patterns for approximating different surfaces.

The mean curvature and the Gauss curvature at every hole are then given by

$$H(u,v) = \frac{eG - 2fF + gE}{2(EG - F^2)} \tag{S37}$$

and

$$K(u,v) = \frac{eg - f^2}{EG - F^2}, \tag{S38}$$

where $E = \langle \mathbf{X}_u, \mathbf{X}_u \rangle$, $F = \langle \mathbf{X}_u, \mathbf{X}_v \rangle$, $G = \langle \mathbf{X}_v, \mathbf{X}_v \rangle$, $e = \langle \mathbf{N}, \mathbf{X}_{uu} \rangle$, $f = \langle \mathbf{N}, \mathbf{X}_{uv} \rangle$, $g = \langle \mathbf{N}, \mathbf{X}_{vv} \rangle$, and $\mathbf{N}$ is the outward unit normal of the Bézier surface.

Figure S12 shows a physical model of a generalized quad kirigami pattern for surface fitting fabricated using Polydimethylsiloxane (PDMS). A mold is first 3D printed to form a negative space of the undeployed pattern. Then, PDMS is poured into the mold, thereby creating a deployable kirigami structure. It can be observed that the deployed shape fits a hat-like surface very well. This shows that our inverse kirigami design is applicable to different materials.

Besides the generalized quad kirigami patterns shown in the main text, we can also consider generalizing the kagome kirigami patterns for surface fitting. The formulation is almost identical to the case of quad pattern, except for that the planarity constraints are automatically satisfied for the case of triangles. Figure S13 shows the surface fitting results with generalized kagome kirigami patterns produced by our method. Again, our approach is capable of fitting surfaces with different curvature properties, and further satisfying additional boundary constraints of the generalized kirigami patterns.

References

[1] Rafsanjani, A., & Pasini, D.. Bistable auxetic mechanical metamaterials inspired by ancient geometric motifs. Extreme Mechanics Letters **9**, 291-296 (2016).

[2] Choi, G. P. T., & Lui, L. M.. A linear formulation for disk conformal parameterization of simply-connected open surfaces. Advances in Computational Mathematics **44(1)**, 87-114 (2018).

[3] Meng, T. W., Choi, G. P. T., & Lui, L. M.. TEMPO: feature-endowed Teichmüller extremal mappings of point clouds. SIAM Journal on Imaging Sciences **9(4)**, 1922-1962 (2016).

[4] Farin, G.E., & Farin, G.. Curves and surfaces for CAGD: a practical guide. Morgan Kaufmann (2002).